- Assessing the cumulative impact of on-farm reservoirs on modeled surface hydrology
- 3 Vinicius Perin<sup>1\*</sup>, Mirela G. Tulbure<sup>2</sup>, Shiqi Fang<sup>3</sup>, Sankarasubramanian Arumugam<sup>3</sup>, Michele L.
   4 Reba<sup>4</sup>, Mary A. Yaeger<sup>5</sup>
- <sup>5</sup> Planet Labs Inc., San Francisco, CA 94107, USA.
- <sup>2</sup> Center for Geospatial Analytics, North Carolina State University, 2800 Faucette Drive, 7 Raleigh, NC 27606, USA
- $^{3}$  Department of Civil, Construction and Environmental Engineering, North Carolina State
- 9 University, 961 Partners Way, Raleigh 27695, USA
- <sup>4</sup> USDA-ARS Delta Water Management Research Unit P.O. Box 2, State University, AR 11 2467-0002, USA.
- 12 <sup>5</sup> Center for Applied Earth Science and Engineering Research, The University of Memphis, 13 3675 Alumni Drive, Memphis, TN 38152, USA.
- 14 \*Corresponding author: vperin@planet.com

15

## 16 Abstract

17

18 On-farm reservoirs (OFRs) are essential water bodies to meet global irrigation needs. Farmers 19 use OFRs to store water from precipitation and runoff during the rainy season to irrigate their 20 crops during the dry season. Despite their importance to crop irrigation, OFRs can have a 21 cumulative impact on surface hydrology by decreasing flow and peak flow. Nonetheless, 22 there is limited knowledge on the spatial and temporal variability of the OFRs' impacts. 23 Therefore, to gain novel understanding on the cumulative impact of OFRs on surface 24 hydrology, here we propose a novel framework that integrates a top-down data driven 25 remote sensing-based algorithm with physically-based models by leveraging the latest 26 developments in the Soil Water Assessment Tool+ (SWAT+). We assessed the impact of OFRs

27 in a watershed located in eastern Arkansas, the third most irrigated state in the USA. Our 28 results show that the presence of OFRs in the watershed can decrease annual flow on 29 average between 14 and 24%, and the mean reduction in peak flow varied between 43 and 30 60%. In addition, the cumulative impact of the OFRs was not equally distributed across the 31 watershed, and it varied according to the OFR spatial distribution, and their storage capacity. 32 The results of this study and the proposed framework can support water agencies with 33 information on the cumulative impact of OFRs, aiming to support surface water resources 34 management. This is relevant as the number of OFRs is expected to increase globally as an 35 adaptation to climate change under severe drought conditions.

36

### 37 1 Introduction

38 Inland water bodies (e.g., lakes and reservoirs) comprise a small fraction of Earth's surface;
39 however, they are responsible for storing the vast majority of the accessible fresh water
40 resources available on Earth. In addition, these water bodies are pivotal components of
41 surface hydrology, having key roles in ecosystem functioning and wildlife habitats (Khazaei et
42 al., 2022; Verpoorter et al., 2014). In particular, on-farm reservoirs (OFRs) are essential to meet
43 global irrigation needs (Döll et al., 2009; Downing, 2010; Van Den Hoek et al., 2019). Farmers
44 use OFRs to store water from precipitation and runoff during the rainy season to irrigate their
45 crops during the dry season (Habets et al., 2018; Perin et al., 2021; Vanthof & Kelly, 2019; Yaeger
46 et al., 2017; Yaeger et al., 2018). The number of OFRs is expected to rise worldwide in the
47 coming decades, and estimates show that there are more than 2.1 million OFRs in the US
48 alone (Downing, 2010; Renwick et al., 2005). OFRs are often built to manage surface water
49 resources more efficiently, and to help mitigate the impact of extreme droughts, which are
50 projected to increase due to climate change (Habets et al., 2018; Van Der Zaag & Gupta, 2008).
51 Although OFRs are small water bodies (< 50 ha), they can have cumulative impacts on the

53 peak flow) (Habets et al., 2018), and their impact may contribute to worsening the surface 54 water stress already intensified by climate change and population growth (Vörösmarty et al., 55 2010). Most studies have focused on the cumulative impact of major large reservoirs on 56 downstream flow alteration (Chalise et al., 2021; Mukhopadhyay et al., 2021), but limited 57 analysis has been performed on the impact of OFRs on downstream flow availability.

To quantify the impact of OFRs on surface hydrology, it is necessary to understand the spatial and temporal variability of OFRs, as well as how the impacts are related to the OFR networks, as the impacts of OFRs are not the sum of the individual OFR impacts, but rather the sum and their interaction effects (Canter & Kamath, 1995; Habets et al., 2018). By gathering information from several studies conducted in different countries (e.g., USA, France, Brazil), Habets et al., (2018) did a thorough assessment of the OFRs' impact on surface hydrology, and the different types of models and ways to represent the OFRs on the watershed. The authors concluded that the modeled OFRs impacts have a wide range, and that most of the studies reported a mean annual reduction in flow, which ranged between 0.2 and 36%. In addition, the variability of the impact as identified in these previous studies was higher when assessing low flows during multiple years, with reductions between 0.3 and 60%. In general, the estimated mean annual reduction in flow was 13.4% ± 8.0%, and the mean decrease in peak flow was up to 45% (Habets et al., 2018).

The approaches used to quantify the cumulative impact of OFRs can be divided into two classes: data-driven methods, and process based hydrological modeling. The data-driven approaches include three main methods. The first method relies on assessing measured inflows and outflows of selected OFRs aiming to quantify their hydrological functioning with the assumption that the cumulative impacts are the sum of individual impacts (Culler et al., 1961; Dubreuil and Girard, 1973; Kennon, 1966). A variation of the cumulative impact assessment approach has been recently suggested by Hwang et al., (2021) by comparing the naturalized flows and the controlled flows for assessing the impact of large reservoir systems.

watershed as the number of OFRs increased (Galéa et al., 2005; Schreider et al., 2002). This approach is limited when discriminating the specific impact of OFRs from those of land use and land cover change, and when explicitly representing the OFRs in the models, given that OFRs tend to be aggregated within the entire basin (i.e., OFRs surface area and/or storage are summed and modeled as a unique water impoundment). The third method relies on conducting a paired-catchment experiment by comparing the flows from two adjacent and similar catchments, one with OFRs and the other without OFRs (Thompson, 2012). This technique requires the catchment properties (e.g., soils, topology, lithology, land cover) to be spatially homogeneous, which is practically nonexistent at a large scale, hence limiting this method's applications.

The second class of methods relate to hydrological modeling, and it is the most widely 90 91 used approach for assessing the OFRs' impacts. A variety of models have been proposed by 92 coupling the OFRs' water balance with a quantitative approach to estimate the OFRs' water 93 volume change (Fowler et al., 2015; Habets et al., 2014; Jalowska & Yuan, 2019; Yongbo et al., 94 2014; Ni & Parajuli, 2018; Perrin, 2012; Zhang et al., 2012). In general, the models have three 95 main components: the OFR water balance, the quantitative approach to quantify the OFR 96 inflows, and the spatial representation of the OFRs network. These different model 97 components result in different limitations and assumptions—a complete assessment of these 98 three components and how they impact the hydrological simulations is provided in a recent 99 review (Habets et al., 2018). Therefore, when selecting a specific model to assess the impacts 100 of the OFRs, it is important to account for the model's suitability for the target issue to be 101 addressed, as well as the model limitations and assumptions. The selected model should also 102 have capability to incorporate/assimilate varying land-surface conditions (e.g., soil moisture) 103 and time-varying OFR storages which could be obtained either from local monitoring or 104 through remote sensing.

Most studies have used remotely-sensed products such as soil moisture (e.g., SMAP; 106 (Entekhabi et al., 2010), groundwater (e.g., GRACE; (Tapley et al., 2004) and land cover

107 conditions (e.g., MODIS; (Justice et al., 1998)) for assimilating current conditions into 108 hydrological models. Given that OFRs tend to occur in high numbers (e.g., hundreds), 109 multiple studies leveraged the latest developments and availability of satellite imagery to 110 monitor the occurrence and dynamics of OFRs (Jones et al., 2017; Ogilvie et al., 2018, 2020; 111 Perin et al., 2022; Perin et al., 2021a, 2021b; Van Den Hoek et al., 2019; Vanthof & Kelly, 2019), 112 which could provide useful information on local storage conditions for predicting 113 downstream streamflow. Further, these studies allowed quantifying the number of OFRs, and 114 their spatial and temporal variability in surface water area and storage in the watershed 115 where they occur, providing relevant information when modeling the cumulative impact of 116 OFRs. Despite the complementary information provided by satellite imagery, there are only a 117 few studies that incorporated remote sensing-derived information (e.g., soil moisture derived 118 from SMAP, groundwater based on GRACE) with hydrological modeling (Ni and Parajuli, 2018; 119 Yongbo et al., 2014; Zhang et al., 2012), and these studies are limited to mapping the OFRs 120 occurrence, or to snapshots of the OFRs conditions (e.g., surface area). To the best of our 121 knowledge, there is no study that combines the spatial and temporal variability of the 122 OFRs—derived using multi-year satellite imagery time series analyses—with a process-based 123 hydrological model.

Therefore, to gain novel understanding of the cumulative impact of OFRs on surface hydrology, in this study, we propose a new approach that systematically integrates the dynamically varying conditions of OFRs based on satellite imagery time series (Perin et al., 2022) using a top-down data driven approach within the latest SWAT+ model. The Soil and Water Assessment Tool (SWAT) (Arnold et al., 2012) has been widely used to model the impacts of the OFRs (Jalowska and Yuan, 2019; Kim and Parajuli, 2014; Ni et al., 2020; Ni and Parajuli, 2018; Perrin, 2012; Rabelo et al., 2021; Yongbo et al., 2014; Zhang et al., 2012), in part given by a comprehensive collection of model documentation and guidelines available online (https://swat.tamu.edu/). Our objectives are to (1) assess the spatial and temporal variability of the cumulative impact of OFRs at the watershed and subwatersheds levels, and (2) to

134 quantify the intra- and-inter annual impacts of the OFRs on flow and peak flow at the 135 channel scale. By integrating the SWAT+ model with a novel remote sensing assimilation 136 algorithm to account for the OFRs spatial variability—which is lacking in most of studies 137 assessing the OFRs impacts—and leveraging a digitally-mapped OFRs dataset (Yaeger et al., 138 2017), we are providing a new approach that can be replicated in watersheds across the 139 world, and used to support water agencies with information to improve surface water 140 resources management.

## 141 2 Methods

### 142 2.1 Study region

143 The study region is located in eastern Arkansas, USA, the third most-irrigated state in the USA 144 (ERS-USDA, 2017). The area has a humid subtropical climate with a 30-year annual average 145 precipitation of ~1300 mm/year (PRISM Climate Group, 2022). The precipitation is distributed 146 mostly between March and May, receiving an average of ~400 mm during these months 147 (Perin et al., 2021b). The region has experienced a steady increase in irrigated agriculture, with 148 commonly irrigated crops including corn, rice, and soybeans (NASS-USDA, 2017). A recent 149 study (Yaeger et al., 2017) digitally mapped 330 OFRs located in the study region (Fig. 1) using 150 the high-resolution (1-m) National Agricultural Imagery Program archive in combination with 151 2015 sub-meter spatial resolution Google Earth satellite imagery. Most of the OFRs (95%) have 152 surface area < 50 ha, and they are concentrated in the eastern portion of the study region 153 (Fig. 1). Currently, there is no comprehensive and up-to-date inventory of all OFRs in the basin. 154 This limitation is partly due to the fact that many of these man-made structures are located 155 on private properties, making them difficult to document. As a result, the study only accounts 156 for a fraction of the total OFRs present in the study region.

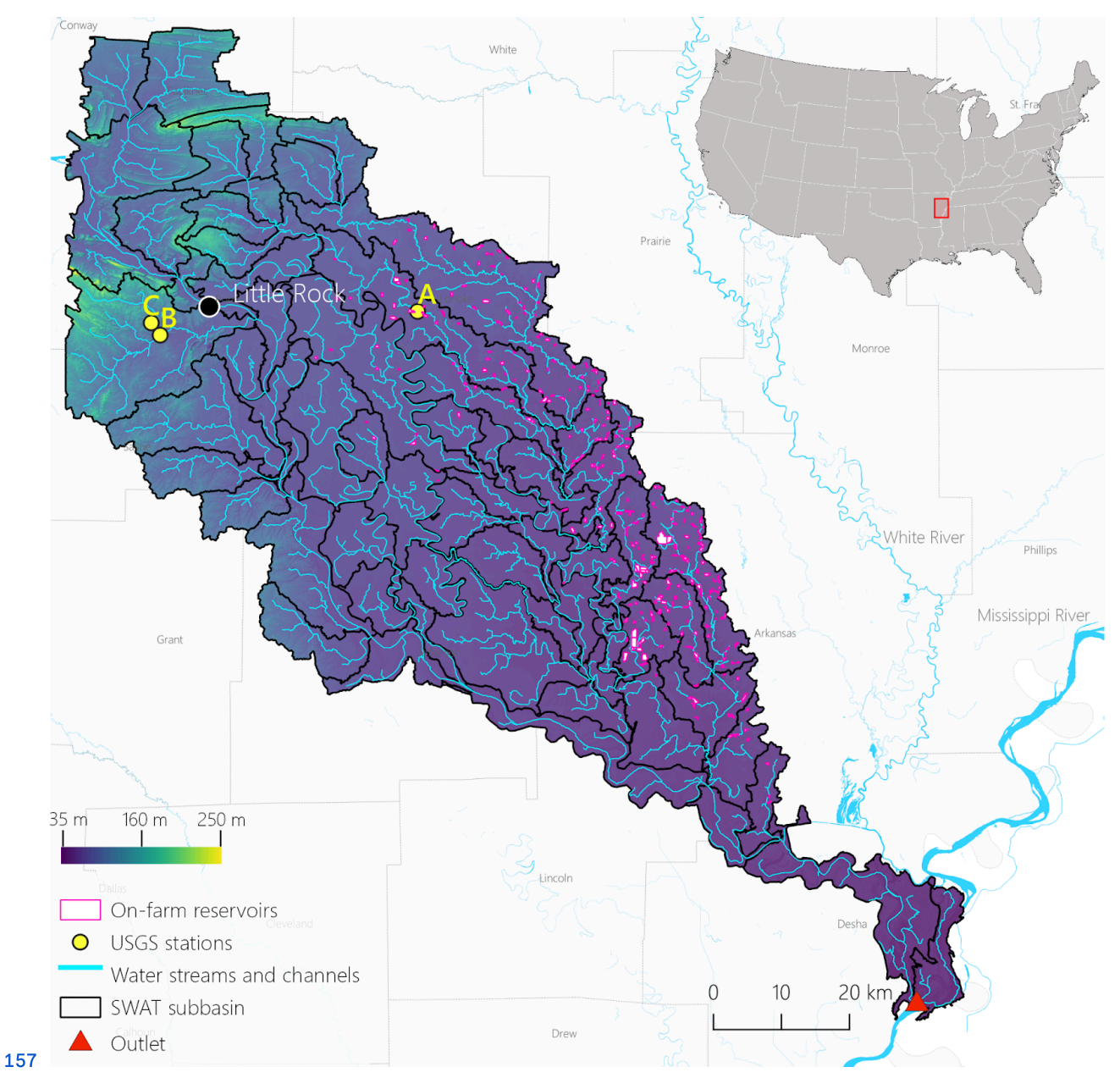


**Figure 1**–Study region located in eastern Arkansas, USA, the subwatersheds and surface water 159 streams and channels delineated with SWAT+, the model outlet, the United States Geological 160 Survey (USGS) stations (United States Geological Survey Water Data for the Nation, 2022) used 161 for flow calibration and validation, the digitized OFRs (Yaeger et al., 2017), and the Digital 162 Elevation Model (DEM) used in the modeling (Farr et al., 2007).

#### 163 2.2 SWAT+ model setup

#### 164 2.2.1 The Soil Water Assessment Tool to model the impacts of OFRs on surface hydrology

165 The SWAT model is a time-continuous semi-distributed hydrological model widely used 166 across the globe—more than 5,000 peer reviewed publications since its launch in the early 167 1980s (Publications | Soil & Water Assessment Tool (SWAT), 2022). The large number of SWAT 168 applications globally revealed the model development needs and its limitations. To address 169 the present and future challenges when modeling with SWAT, the model source code has 170 undergone major modifications, and a completely revised version of the model was proposed 171 in SWAT+ (Bieger et al., 2017). SWAT+ uses the same equations as SWAT to simulate the 172 hydrological processes; however, it offers more flexibility to users when configuring the model 173 (e.g., when defining management schedules, routing constituents, and connecting managed 174 flow systems to the natural stream network) (Bieger et al., 2017).

The SWAT+ is under constant improvements (Chawanda et al., 2020; Molina-Navarro et 176 al., 2018), and a new module (Molina-Navarro et al., 2018) was recently developed to allow the 177 optimal integration of a water body and its drainage area within the simulated hydrological 178 processes. In previous versions of the model, when delineating the watershed area draining 179 into a water body, the users were required to place an outlet in a certain point of the water 180 stream's network, and the areas in-between the rivers' subwatersheds flowing into the water 181 body were therefore excluded—if these areas are disregarded, important hydrological 182 processes (e.g., evaporation, overland and/or groundwater flow) flowing into the water body 183 are not accounted for (Molina-Navarro et al., 2018). This former approach can lead to 184 inaccuracies when delineating the watershed areas, especially when the results are used as 185 input to an OFR model component. The newest versions of SWAT+ consider the OFRs' outline 186 (i.e., shape and surface area) when delineating the watersheds; hence, accounting for the 187 entire drainage area flowing into the waterbody (Mollina-Navarro et al., 2018). In addition, the 188 latest versions allow adding more than one OFR per subwatershed by associating the OFR

189 with channels—components of the watersheds, and finer divisions and extensions of water 190 stream reaches—enabling the modeling analyses at the channel scale. When simulating the 191 impact of the OFRs at the channel scale, there is a higher level of detail of where and when 192 the OFRs are contributing to changes in surface hydrology, unlike the previous versions of the 193 model, which allowed adding only a single OFR per subwatershed placed at the 194 subwatershed outlet as a point (Arnold et al., 2012), and therefore, the analyses were 195 conducted at the subwatershed scale.

We modeled the impact of OFRs on surface hydrology using the QSWAT+ (v.2.1.9) 197 SWAT+ model interface together with SWAT+ Editor (v.2.1.0) to set up the model, to input the 198 required datasets (e.g., DEM, land use and land cover layer, interpolated meteorological 199 climate information), and to run the different modeling scenarios.

The modeled watershed (710,700 ha, Fig. 1) included 68 subwatersheds and a total of 200 201 642 Hydrological Response Units (HRUs)—HRUs are unique portions of the subwatersheds 202 that have unique land use and management, and soil attributes. We set up daily simulations 203 for 30 years (1990-2020), including five years of model warm up to establish the initial soil 204 water conditions and hydrological processes. The watershed was delineated using the Shuttle 205 Radar Topography Mission DEM (30 m) (Farr et al., 2007). In addition, we set the channel 206 length threshold to 6 km<sup>2</sup>, and the stream length threshold to 60 km<sup>2</sup>. We placed an outlet in 207 the southern part of the study region—where the lowest part of the watershed is located (Fig. 208 1). We created the HRUs using the dominant option—this option selects the largest HRU 209 within the subwatershed as the general HRU—within QSWAT+ interface, and used the 210 National Land Cover Database (30 m) (Homer et al., 2020), and Gridded Soil Survey 211 Geographic Database (gSSURGO) (Soil Survey Staff, USDA-NRCS, 2021) (100 m) as inputs to 212 the model. The gSSURGO layers were processed according to their guidelines when using 213 them on QSWAT+ (George, 2020). For climate data, we extracted the centroid coordinates of 214 each subwatershed (Muche et al., 2020), and used these centroids to download 30 years of 215 daily precipitation, minimum and maximum temperature, surface downward shortwave 216 radiation, wind velocity, and relative humidity from the Gridded Surface Meteorological 217 Datasets (Abatzoglou, 2013), available in Google Earth Engine (Gorelick et al., 2017). The time 218 series of each subwatershed centroid was added into the SWAT+ Editor as independent 219 weather stations.

### 220 2.2.2 Model calibration and validation procedures

221 We used monthly measured flow from three USGS stations (Fig. 1 and Table 1) to calibrate and 222 validate the model flow simulations. The USGS flow time series length varied between 14 and 223 25 years, and we used 60% of the timeseries for calibration and 40% for validation for each 224 USGS station (Table 1). We assessed the performance of the model by calculating the 225 Coefficient of determination (r<sup>2</sup>), Percent bias (PBIAS, %, Equation 1) (Yapo et al., 1996), and the 226 Nash-Sutcliffe model efficiency coefficient (NSE, Equation 2) (Nash and Sutcliffe, 1970). PBIAS 227 is the relative mean difference between the simulated and the measured flow values, and it 228 reflects the ability of the model to simulate monthly flows. The optimal PBIAS is zero, and 229 low-magnitude values indicate better model performance. Positive PBIAS indicates 230 overestimation bias, whereas negative values denote underestimation bias. The NSE 231 expresses how well the model simulates flows, and it ranges from a negative value to one, 232 with one indicating a perfect fit between the simulated and measured flow values. In general, 233 the model simulations of monthly flow are considered satisfactory when r<sup>2</sup> ranges from 0.60 234 to 0.75, PBIAS ranges from ±10% to ±15%, and NSE ranges from 0.50 to 0.70 (Moriasi et al., 2015). 235 Table 1-USGS stations, drainage areas, and the periods used for flow calibration and 236 validation.

USGS station	Station id	Drainage Area (ha)	Period (years)	
			Calibration	Validation
07264000	(A)	53,600	1995–2010	2010–2020
07263555	(B)	25,400	2007–2014	2014–2020
07263580	(C)	5,300	1997–2011	2011–2020

238 PBIAS = 
$$\frac{\sum_{i=1}^{n} (Yi - Xi)}{\sum_{i=1}^{n} Xi}$$
 (1)

239 NSE = 
$$1 - \frac{\sum\limits_{i=1}^{n} (Xi - Yi)^2}{\sum\limits_{i=1}^{n} (Xi - \overline{Xi})^2}$$
 (2)

240 Where  $X_i$  is the measured flow and  $Y_i$  is the simulated flow.

We conducted a sensitivity analysis using the SWAT+ ToolBox (v.0.7.6) (SWAT+ Toolbox, 2022) to reveal the most sensitive parameters when simulating flow—a total of 10 parameters (Table S I) were tested based on previous studies that used SWAT/SWAT+ to model the impact of water impoundments on surface hydrology (Jalowska & Yuan, 2019; Yongbo et al., 2014; Ni et al., 2020; Ni & Parajuli, 2018; Perrin, 2012; Rabelo et al., 2021; Zhang et al., 2012). Following the sensitivity analysis, we selected the five most sensitive parameters (Table 2), and proceeded with a manual calibration using the SWAT+ Toolbox. We aimed to improve the model's monthly flow predictions by testing the parameters one at a time and changing their values between -20% to 20% with 5% increments based on their range values. The final calibrated parameters and their fitted values are shown in Table 2.

251 **Table 2**-Monthly flow calibration parameters.

Parameter	Description	Range	Value
CN2	SCS runoff curve number	35–95	0.20*
SOL_AWC	Available water capacity (mm/mm)	0.01–1	-0.20*
ESCO	Soil evaporation compensation coefficient	0.01–1	0.50
PERCO	Percolation coefficient (fraction)	0–1	0.60
CANMX	Maximum canopy storage (mm)	0–100	75

<sup>252 \*</sup>Denotes relative percentage change.

#### 253 2.3 OFRs representation in SWAT+

254 Multiple OFRs can be added to the same subwatershed by associating them with channels 255 (Dile et al., 2022). The OFRs need to have at least one outlet channel, and they may have none 256 or multiple inlets. Therefore, most OFR-related processes within the model involve 257 determining what channels form inflowing and outflowing channels for each OFR. Ideally, 258 each OFR would interact with a channel, and therefore, have a channel entering, leaving, or 259 within the OFR. Nonetheless, it is common to have OFRs that do not intersect with any 260 channel (Dile et al., 2022)—this is the case for 93% of the OFRs in our study region. The OFRs 261 from our study region are not dammed along the streams, but rather they are engineered 262 water impoundments that are indirectly connected to the main streams via pipes and pumps 263 (Yaeger et al., 2017). A possible solution would be modifying the OFRs' shapes by dragging 264 them to the closest channel (Dile et al., 2022). However, this would require extensive 265 modifications of the OFRs' shapes. In addition, when an OFR is added to a channel, this 266 channel is split into two channels, and the model needs to account for the two newly created 267 channels during the water routing calculations. For this reason, adding multiple OFRs to the 268 same channel, or adding multiple OFRs closely located to the same channel, can be a 269 cumbersome process that leads to numerous routing errors.

To overcome these challenges, we aggregated the OFRs' surface area, and added aggregated OFRs to the model. This adaptation involved two steps. First, for each of the 330 PRS, we searched for the closest channel by calculating the distance between the OFRs' centroid and the multiple channels within each subwatershed. Then, we aggregated all the OFRs that were associated with each channel by summing up their surface area, and adding a polygon of the aggregated area to represent the aggregated OFR. This approach resulted in G9 aggregated OFRs that were added to G7 different channels located in 16 subwatersheds. The surface area of the aggregated OFRs varied between 3.05 ha and 165.67 ha, and the number of OFRs in each aggregated OFR varied between 2 and 12. To avoid confusion, for the rest of the manuscript, we refer to OFRs as the aggregated OFRs, and not the individual OFRs shown in Fig. 1.

#### 281 2.4 OFRs water balance

We did not have access to water abstraction data from the OFRs, so all abstractions were modeled using Equation 3, which accounts for water flowing out of the OFR, as well as losses from evaporation and seepage. The total volume of water in the OFR fluctuates with changes in surface area and is also influenced by evaporation losses and the spillway. A reduction in surface area (Equation 4) typically leads to a corresponding decrease in water volume. If inflows are insufficient to fill the OFR, water will not be routed to the downstream changes.

For each of the aggregated OFR, the initial water volume ( $V_{\text{stored}}$ , see Equation 3) was 290 calculated using SWAT+ default rule, which is a simple multiplication of the OFR surface area 291 by a factor of 10, similar to other studies based on SWAT+ (Ni and Parajuli, 2018; Zhang et al., 292 2012). For a scenario where the OFR has a surface area of 1 hectare (10,000 m<sup>2</sup>), the 293 corresponding volume would be 100,000 m<sup>3</sup>—this is an important limitation of our study, as 294 the assumption was necessary due to the absence of available bathymetry data. In addition, 295 given that we did not have access to the OFRs release rates, we used the model default 296 release rule, which sets the OFRs to release water when the spillway volume is reached—80% 297 of the OFRs capacity (Bieger et al., 2017).

$$V = V_{\text{stored}} + V_{\text{flowin}} - V_{\text{flowout}} + V_{\text{pcp}} - V_{\text{evap}} - V_{\text{seep}}$$
(3)

299 Where V is the volume of water in the OFR at the end of the day (m<sup>3</sup>),  $V_{\text{stored}}$  is the volume of 300 water stored at the beginning of the day (m<sup>3</sup>),  $V_{\text{flowin}}$  is the volume of water entering the OFR 301 during the day (m<sup>3</sup>),  $V_{\text{flowout}}$  is the volume of water flowing out of the OFR (m<sup>3</sup>),  $V_{\text{pcp}}$  is the 302 volume of precipitation falling on the water body (m<sup>3</sup>),  $V_{\text{evap}}$  is the volume of water removed 303 from the OFR due to evaporation, and  $V_{\text{seep}}$  is the volume of water lost by seepage (m<sup>3</sup>).

The OFR surface area is used to calculate the amount of precipitation falling on the water body, and the amount of water lost through evaporation and seepage. Given the initial OFR surface area obtained from one of the three modeling scenarios, the OFR surface area was modeled daily. The surface area varied according to the volume of water stored in the reservoir. Equation 4 is used to estimate the surface area:

309 Surface area (ha) = 
$$\beta_{sa} * V^{expsa}$$
 (4)

310 expsa = 
$$\frac{log10 (Vem) - log10 (Vpr)}{log10 (Surface areaem) - log10 (Surface Areapr)}$$
 (5)

311 
$$\beta_{sa} = \left(\frac{Vem}{Surface\ areaem}\right)^{expsa}$$
 (6)

312 Where  $\beta_{sa}$  is a surface area coefficient,  $V_{em}$  is the volume of water (m<sup>3</sup>) at the emergency 313 spillway,  $V_{pr}$  is the volume of water (m<sup>3</sup>) at the principal spillway, *Surface area*<sub>em</sub> is the surface 314 area (ha) at the emergency spillway, and *Surface area*<sub>pr</sub> is the surface area at the principal 315 spillway.

316 The volume of precipitation falling into the OFR is calculated using Equation 7:

317 
$$V_{pcp} = 10 * R_{day} * Surface Area (ha)$$
 (7)

318 Where  $R_{day}$  is the amount of precipitation falling into the OFR on a given day (mm).

319 Evaporation losses are calculated using Equation 8:

320 
$$V_{\text{evap}} = 10 * \eta * E_0 * Surface Area (ha)$$
 (8)

321 Where  $\eta$  is an evaporation coefficient (0.6), and  $E_o$  is the potential evapotranspiration for a 322 given day (mm).

323 Seepage losses are calculated using Equation 9:

324 
$$V_{\text{seep}} = 240 * K_{\text{sat}} * Surface Area (ha)$$
 (9)

325 Where  $K_{sat}$  is the effective saturated hydraulic conductivity of the reservoir bottom (mm/hr).

### 326 2.4 Scenario Analysis

327 Given our representation of the OFRs in SWAT+, we assessed the impact of the OFRs on 328 surface hydrology at the channel scale. To do so, we established the model baseline scenario 329 without the presence of the OFRs on the watershed. In addition, we divided the channels into 330 four classes (i.e., low and high flow classes) according to their mean baseline flow. The 331 different class intervals were calculated using the mean flow quartiles accounting for all 332 channels, which resulted in the following baseline flow classes: (1) 0.001–0.25 m<sup>3</sup>/s, (2) 0.25–0.50 333 m<sup>3</sup>/s, (3) 0.50–2.11 m<sup>3</sup>/s, and (4) 2.11–17.50 m<sup>3</sup>/s.

To account for the OFRs variation in surface area (i.e., change in storage capacity), we 334 335 propose a novel approach that leverages a top-down data-driven model based on satellite 336 imagery (Fig. 2). We used this model to create three modeling scenarios using daily OFRs 337 surface area time series—these scenarios were based on the methodology proposed by Perin 338 et al., (2022). The authors used a multi-sensor satellite imagery approach with the Kalman 339 filter (Kalman, 1960) to derive daily OFRs' surface area change between 2017 and 2020. The 340 proposed algorithm accounts for the uncertainties in both the sensor's observations and the 341 resulting surface areas. By improving the OFRs surface area observations cadence, the 342 algorithm allows further understanding of the OFRs surface area intra- and inter-annual 343 changes, which are key pieces of information that can be used to better assess and manage 344 the water stored by the OFRs (Perin et al., 2022). The daily surface area time series—derived by 345 combining PlanetScope, RapidEye, and Sentinel-2 satellite imagery (Perin et al., 2022)—of 346 each OFR was used to simulate three scenarios (i.e., lower, mean, and upper) representing the 347 OFRs' capacity in terms of surface area. The mean scenario represents the regular condition 348 of the OFRs, and it is the mean of the daily surface area time series derived from the Kalman 349 filter. The lower and upper scenarios represent the lowest and highest capacities of the OFRs, 350 and they are based on the surface area 95% confidence interval limits, calculated using the 351 daily time series. Please refer to Perin et al., 2022 for more details on how the 95% confidence 352 interval was calculated.

The SWOT+ model does not allow for direct incorporation of a daily surface area time series because it calculates surface area dynamically (Equation 4) based on changes in water stollars volume through the reservoir water balance equation (Equation 3). It is structured to accept a single surface area value per scenario, which then varies internally. Incorporating time-varying surface area data, such as from the Kalman filter, would require modifications to the model that are currently not supported. Therefore, a single surface area value was assigned to each scenario and OFR, with lower, mean, and upper values used as starting points for the model's water balance simulations. This initial surface area reflects the OFR's maximum surface area for the full capacity for each scenario. For example, in the lower scenario, an initial surface area of 1.2 ha represents the maximum area for this OFR. As model iterations proceed, the surface area is recalculated based on Equation 4. The initial OFR capacity was surface area.

For each scenario, a single value of the OFRs surface area was set during the the OFRs were simulated at full capacity (i.e., maximum storage at the lower, mean and upper seenarios), and this capacity was kept constant during the simulation period (Ni et al., 2020; Ni and Parajuli, 2018; Perrin, 2012). In other words, the OFR surface area varied according to seenarion 4, however, the maximum surface area did not exceed the initial value. To assess the impact of the OFRs on surface hydrology, we compared the baseline flow with the flow simulated by each surface area scenario—i.e., comparing the flow changes with and without OFRs, a common approach used by previous studies (Habets et al., 2018).

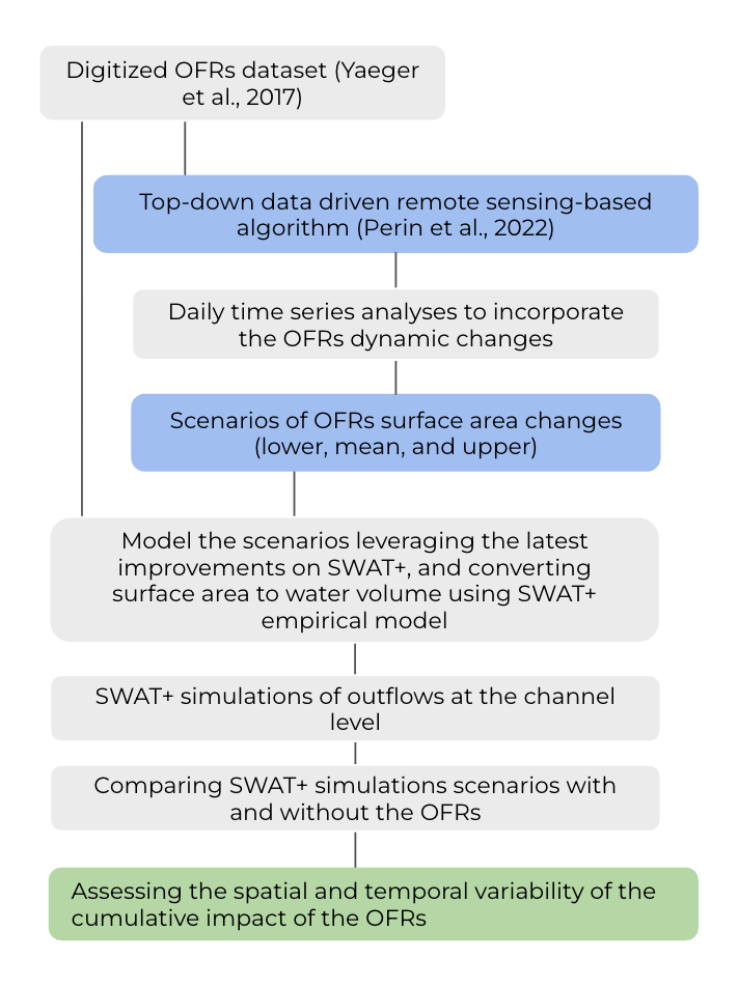


**Figure 2**–A new approach to integrate a top-down data driven remote sensing-based 374 algorithm, that assesses the OFRs dynamic conditions (Perin et al., 2022), with the latest 375 SWAT+ model developments.

We estimated the impact of the OFRs on surface hydrology by calculating the percent change (Equation 10) of monthly flow between the baseline and the three surface area scenarios including all OFRs. The annual impact on flow was calculated by averaging the mean percent change along the months. We also calculated the distribution of the percent change for each baseline flow class. The distribution was assessed using 2-D Kernel Density estimation (KDE) plots. Different from discrete bins (e.g., histograms), the KDE plots show a continuous density estimate of the observations using a Gaussian kernel. In addition, we assessed the percent changes in peak flow. For the purposes of this analysis, peak flow is defined as equal or higher than the 99<sup>th</sup> flow percentile calculated using the entire flow time

385 series (Equation 10). It is important to keep in mind that the impact of the OFRs on this study 386 is solely based on modeling scenarios and does not account for OFR management practices, 387 which represents a key limitation of this simulation study.

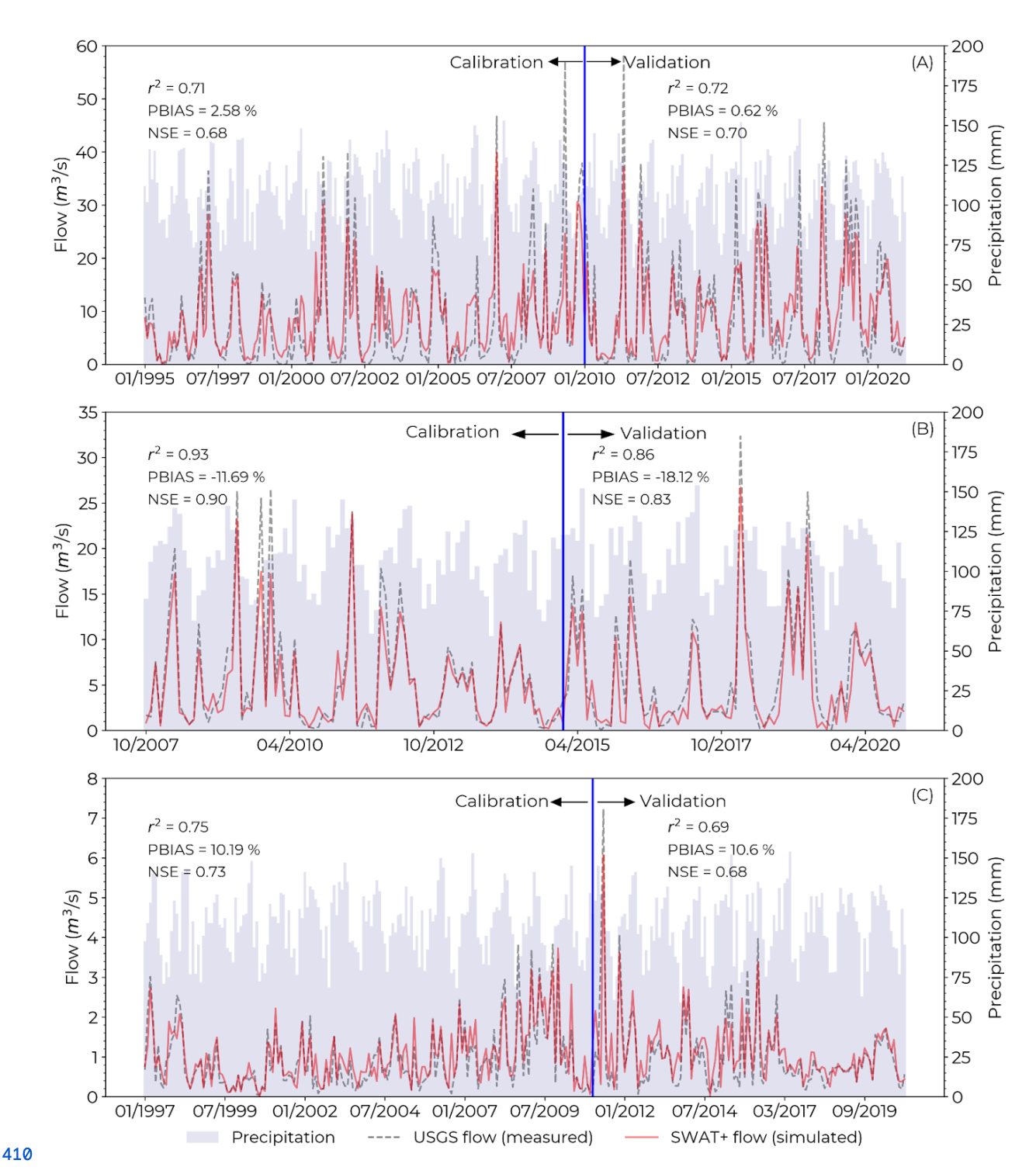
388 Percent change (%) = 
$$\left(\frac{Yi - Xi}{Xi}\right)$$
 \* 100

389 Where  $X_i$  is the baseline flow and  $Y_i$  is the simulated flow of each surface area scenario.

## 390 3 Results

#### 391 3.1 Model calibration and validation

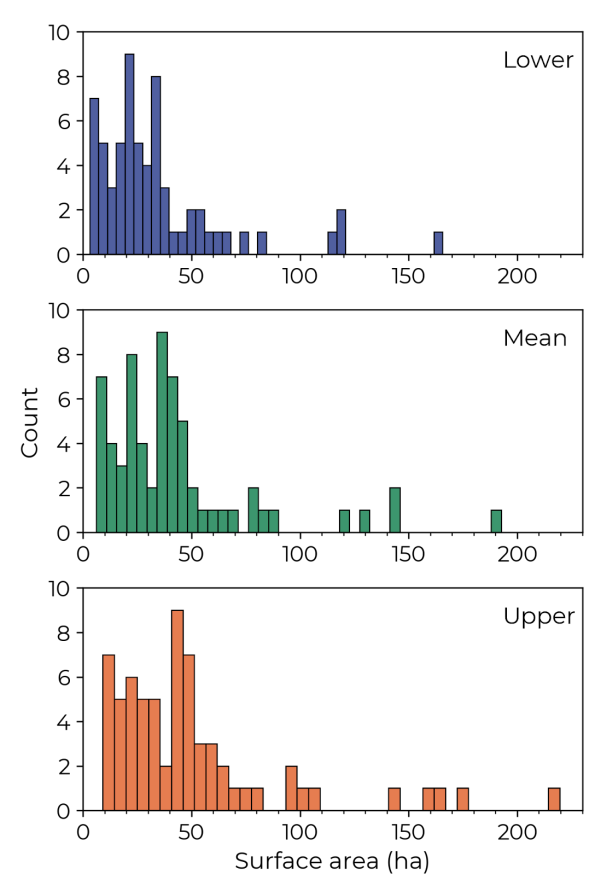
392 The model calibration and validation were done using the three USGS stations presented in 393 Fig. 1 and Table 1, and accounting for all OFRs in study region. When comparing the monthly 394 simulated flow with the measured flow for the calibration period, there was a good 395 agreement (0.71 ≤  $r^2$  ≤ 0.93), and a satisfactory model efficiency (0.68 ≤ NSE ≤ 0.90) for all three 396 stations (Fig. 3). In addition, the PBIAS magnitude was < 3% for station A, and < 12% for 397 stations B and C. Meanwhile, the validation period had r<sup>2</sup> ranging between 0.69 and 0.86, and 398 the NSE between 0.68 and 0.83, with PBIAS magnitude < 10% for stations A and B, and 18.12% 399 for station C. In general, for stations A and C, the model overestimated flow values (i.e., 400 positive PBIAS) mostly during flow events  $< 3 \text{ m}^3/\text{s}$ , and the model underestimated flow (i.e., 401 negative PBIAS) for station B during flows > 20 m<sup>3</sup>/s (Fig. 3). These findings are consistent 402 with a previous study conducted in western Mississippi near our study region (Ni and Parajuli, 403 2018). Even though during the validation period the station B had PBIAS magnitude higher 404 than 15%, the r<sup>2</sup> and NSE values from the calibration and validation periods indicate 405 satisfactory modeling performance when simulating monthly flow (Moriasi et al., 2015). Given 406 that none of the OFRs were directly connected with the streams where the stations were 407 located (Fig. 1), and there were no OFRs nearby stations B and C, the calibration and 408 validation metrics with and without the OFRs were very similar, with differences smaller than 409 1%.



**Figure 3**–Flow calibration and validation time series for the three USGS stations A (07264000), 412 B (07263555) and C (07263580). See Fig. 1 and Table 1 for more information about the USGS 413 stations. The precipitation time series represents the monthly accumulated precipitation at 414 the watershed scale (i.e., for the entire study region).

## 415 3.2 Percent change in flow

416 We assessed the impact of the OFRs on flow by comparing the baseline flow (i.e., without the 417 OFRs) with the three surface area scenarios generated from the Kalman filter 418 approach—lower, mean, and upper (see section 2.4, and Fig. 2). The total surface area (i.e., 419 summing all OFRs surface area) was 2.176 ha for the lower, 2.766 ha for the mean, and 3.370 420 ha for the upper, and the three scenarios had a similar OFRs surface area distribution (Fig. 4). 421 In addition, most of the OFRs had surface areas < 50 ha—78%, 71%, and 62% of the OFRs for 422 the lower, mean, and upper scenarios.



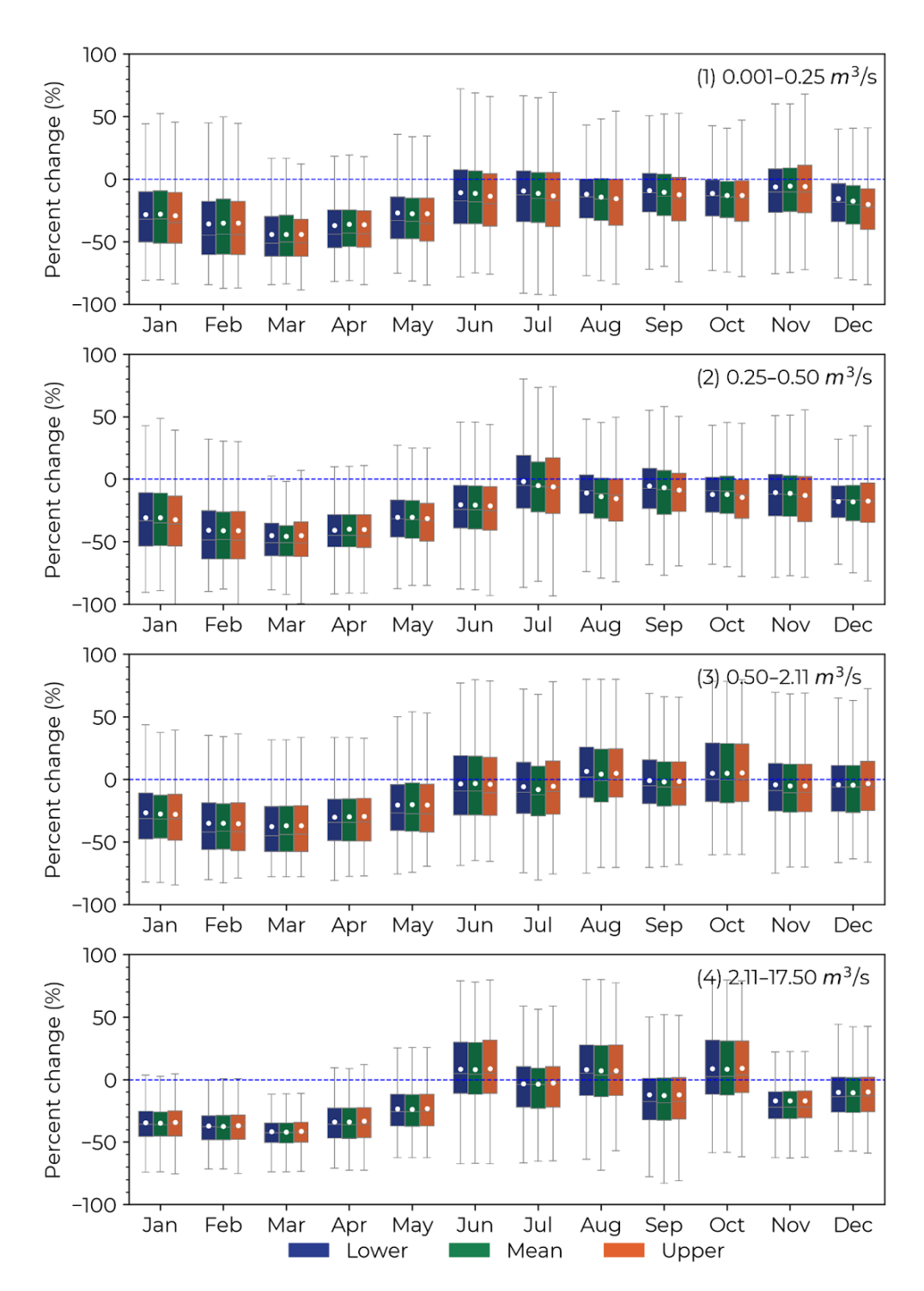
424 **Figure 4**–OFRs surface area distribution for the three surface area scenarios, lower, mean, and 425 upper.

Figure 5 breaks down the channels into four distinct categories, with each category 427 showing percent changes in flow throughout the year, displayed along the x-axis by month. 428 The three bar colors represent different scenarios, while bar heights illustrate variations across

429 channels and years. For example, the bars for January include all January data spanning from 430 1990 to 2020, enabling a thorough comparison of seasonal and year-to-year flow changes. The 431 impact of the OFRs on monthly flow varied throughout the year, and the largest impacts 432 occurred between January and May for all flow classes (Fig. 5). During these months, 433 including all surface area scenarios, the mean decrease in flow (i.e., negative mean percent 434 change) was  $-34.4 \pm 6\%$  for class 1,  $-37.6 \pm 5\%$  for class 2,  $-30.0 \pm 6\%$  for class 3, and  $-34.1 \pm 6\%$  for 435 class 4. For all classes, the greatest reduction in flow occurred during the month of March (-436 -40%). Meanwhile, the impact of the OFRs was smaller during the second half of the year, in 437 which the mean percent change in flow was  $-12.0 \pm 3.\%$  for class 1,  $-12.5 \pm 5\%$  for class 2,  $-1.4 \pm 438$  4% for class 3, and  $-2.6 \pm 10\%$  for class 4 (Fig. 5). So we always saw a decrease? It looks like we 439 have some increases too.

When assessing the mean percent change per month, for all surface area scenarios, 441 the lower flow classes (i.e., (1)  $0.001-0.25 \text{ m}^3/\text{s}$  and (2)  $0.25-0.50 \text{ m}^3/\text{s}$ ) had a negative mean 442 percent change for all months. Nonetheless, we observed a mean positive percent change 443 (i.e., increase in flow) for the months of August ( $5.0 \pm 1\%$ ) and October ( $5.2 \pm 0.2\%$ ) for class 3, 444 and during June ( $8.2 \pm 0.3\%$ ), August ( $7.3 \pm 0.4\%$ ), and October ( $8.7 \pm 0.4\%$ ) for class 4 (Fig. 5). 445 Furthermore, the different surface area scenarios had similar impacts on flow for all months 446 of the year with differences smaller than 5% for all scenarios. Between January and May, for all 447 flow classes, the mean percent change was  $-32.0 \pm 6\%$  for the lower,  $-34.6 \pm 7\%$  for the mean, 448 and  $-35.8 \pm 5\%$  for the upper. Between June and December, the impact on flow was  $-5.4 \pm 6\%$  449 for the lower,  $-7.3 \pm 8\%$  for the mean, and  $-8.9 \pm 5\%$  for the upper.

450



**Figure 5**–Monthly percent change in flow between the baseline scenario (vertical dotted blue 454 line) and the three surface area scenarios (lower, mean, and upper), and for the four flow 455 classes (1) 0.001–0.25 m<sup>3</sup>/s, (2) 0.25–0.50 m<sup>3</sup>/s, (3) 0.50–2.11 m<sup>3</sup>/s, and (4) 2.11–17.50 m<sup>3</sup>/s. This 456 analysis included data from all simulated years (1990–2020).

In general, the OFRs contributed to decreased monthly flow. However, the OFRs' 458 impact on flow had a significant intra- and inter-annual variability, and it varied according to 459 different OFRs and channels—this is highlighted by the boxplots size variability in Fig. 5, in 460 which the variability was lower during the first part of the year, and greater between July and 461 August. In addition, the monthly percent change in flow in the KDE plots (Fig. 6) shows that 462 for the three scenarios, and all flow classes, most of the changes in flow ranged between -40% 463 and 0%. In addition, all KDE plots have a triangular shape with its base on the smaller flows, 464 denoting where most of the changes occur. Even though the majority of the percent change 465 in flow is negative, there are circumstances in which the OFRs could positively impact 466 flow—the increase in flow is represented by faded colors in each surface area scenario (Fig. 6). 467 The positive mean percent change could be as high as 80%—see Fig. 6 for the larger flow 468 classes, (3) 0.50–2.11 m³/s and (4) 2.11–17.50 m³/s. The positive impact on flow for these classes 469 occurred during the months of June, August and October when a mean positive change is 470 observed (Fig. 5 classes 3 and 4).

The annual mean percent change, for all surface area scenarios, was -22.5  $\pm$  3% for class 472 1, -24.2  $\pm$  4% for class 2, -14.6  $\pm$  3% for class 3, and -16.6  $\pm$  3% for class 4. In addition, the surface 473 area scenarios annual changes were -18.0  $\pm$  5% for the lower, -19.6  $\pm$  5% for the mean, and -20.8 474  $\pm$  6% for the upper, including all flow classes. The differences between the surface area 475 scenarios shown in Fig. 5 and Fig. 6 are related to the variability of the OFRs surface area.

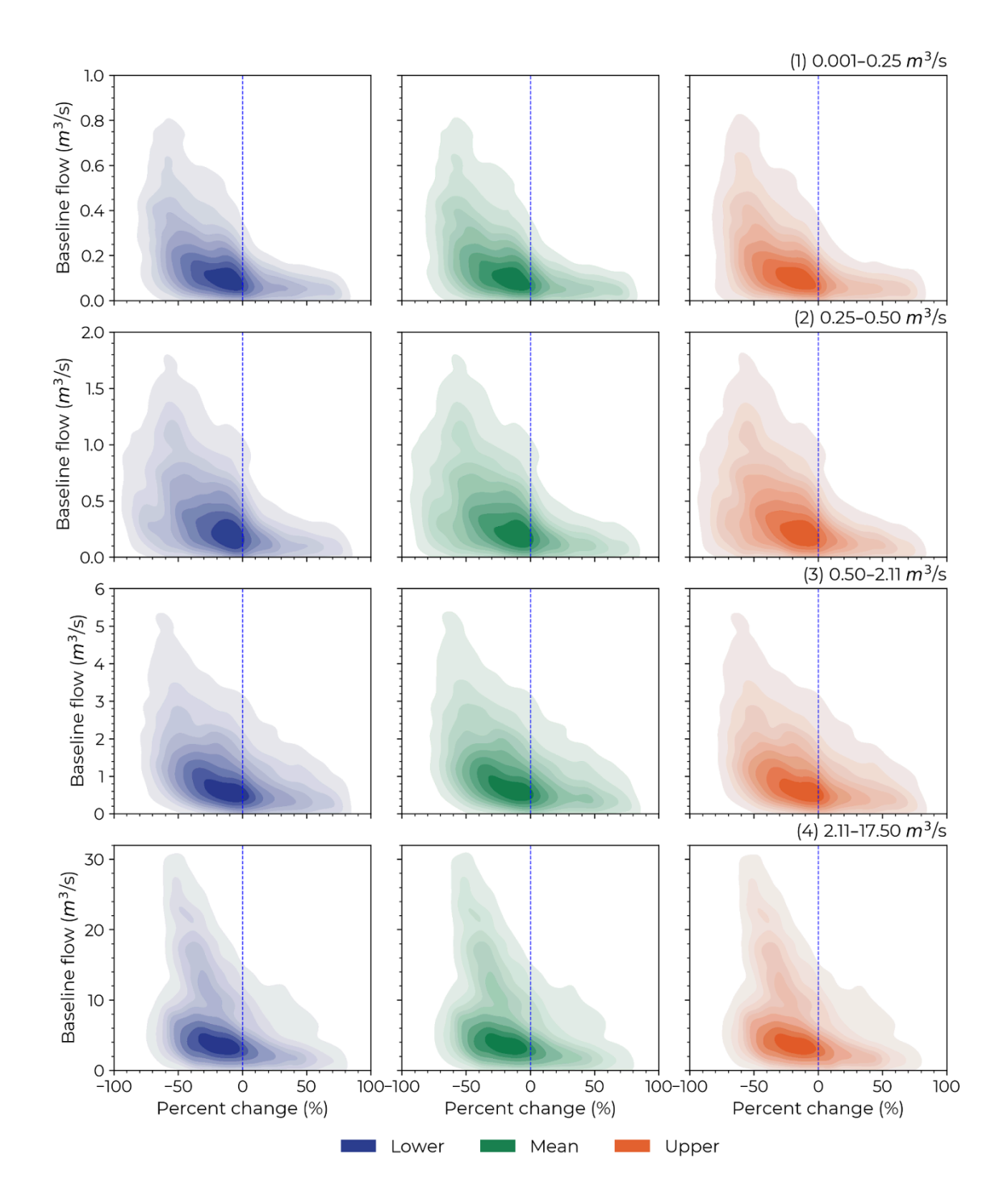


**Figure 6**–Kernel density estimation plots smoothed using a Gaussian kernel for the monthly 482 percent change in flow between the baseline scenario (vertical dotted blue line) and the 483 three surface area scenarios (lower, mean, and upper) for the four flow classes (1) 0.001–0.25

 $\text{m}^3/\text{s}$ , (2) 0.25–0.50  $\text{m}^3/\text{s}$ , (3) 0.50–2.11  $\text{m}^3/\text{s}$ , and (4) 2.11–17.50  $\text{m}^3/\text{s}$ . Note the different range of 485 values on the y-axis for all four flow classes.

### 486 3.3 Impact on peak flow

487 For each channel, we calculated the impact of the OFRs on peak flow (Fig. 7). The impact on 488 peak flow was -60.7  $\pm$  13% for class 1, -56.2  $\pm$  11% for class 2, -46.7  $\pm$  19% for class 3, and -43.9  $\pm$  489 12% class 4. When assessing the impact on peak flow based on different surface area 490 scenarios, the mean percent change was -49.4  $\pm$  18% for the lower, -50.4  $\pm$  17% for the mean, 491 and -52.7  $\pm$  18% for the upper. All peak flows occurred between January and May, which is the 492 period of the year when the study region receives most of its precipitation (Perin et al., 2021). 493 With the exception of a few outliers, there was no increase in peak flow, even though the 494 OFRs contributed to a positive mean percent change in flow in certain months of the year 495 (Fig. 5 classes 3 and 4).

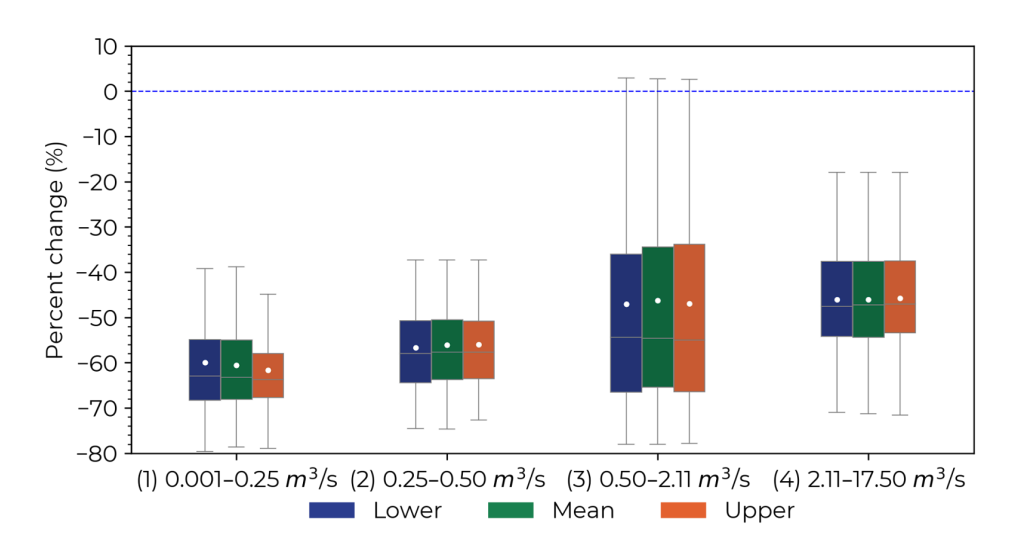


**Figure 7**–Percent change in peak flow between the baseline scenario (vertical dotted blue 498 line) and the three surface area scenarios (lower, mean, and upper) for the four flow classes (1) 499 0.001–0.25 m<sup>3</sup>/s, (2) 0.25–0.50 m<sup>3</sup>/s, (3) 0.50–2.11 m<sup>3</sup>/s, and (4) 2.11–17.50 m<sup>3</sup>/s.

#### 500 3.4 Simulated flow time series

501 We randomly selected a channel within the flow class 3 to demonstrate the baseline and the 502 three surface area scenarios' flow time series between 1995 and 2005 (Fig. 8). For this channel, 503 the annual mean percent changes in flow when comparing the baseline scenario with the 504 lower, mean, and upper surface area scenarios were 0.99 ± 11.8%, -1.9 ± 13%, and -2.0 ± 19%—the 505 high standard deviation for the three scenarios is explained by the interannual variability. The 506 upper surface area scenario resulted in lower flows (i.e., higher impact) when compared to the 507 lower and mean scenarios for the majority of the flow events—67.8% and 57.6% for the lower 508 and mean scenarios. Nonetheless, there are circumstances when the upper scenario yielded 509 higher flows—32.2% and 42.4% of the events for the lower and mean scenarios (e.g., see the 510 two insets 03/1997-08/1998 and 05/2002-02/2004). These findings indicate that the impacts 511 that the OFRs have on flow are not entirely governed by the presence and surface area of the 512 OFRs (i.e., the different surface area scenarios), instead by a combination of the OFRs with 513 different modeling components (e.g., terrain, land use, climate information), and different 514 hydrological processes (e.g., run-off, precipitation, evaporation). In addition, the impact on 515 peak flow for this channel was -45.7 ± 19.7% for all surface area scenarios—this is highlighted 516 on two occasions (08/2002 and 08/2003) during the second inset.

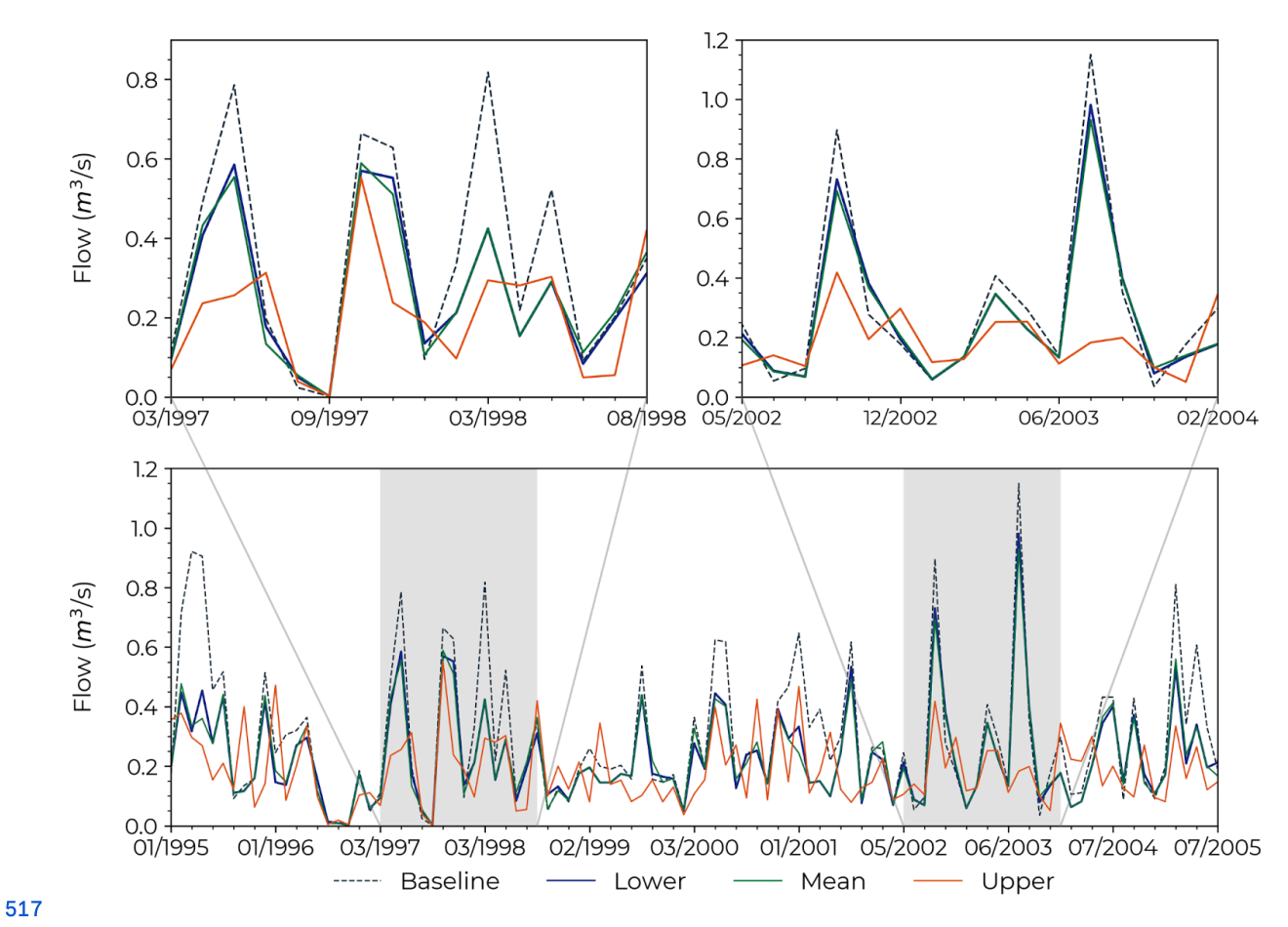


**Figure 8**–A subset of the time series of simulated flow for baseline and the three surface area 519 scenarios (lower, mean, and upper) between 1995 and 2005 for a selected channel within the 520 flow class 3.

530 3.5 Spatial variability of the OFRs impact on annual flow Overall impact of OFRs

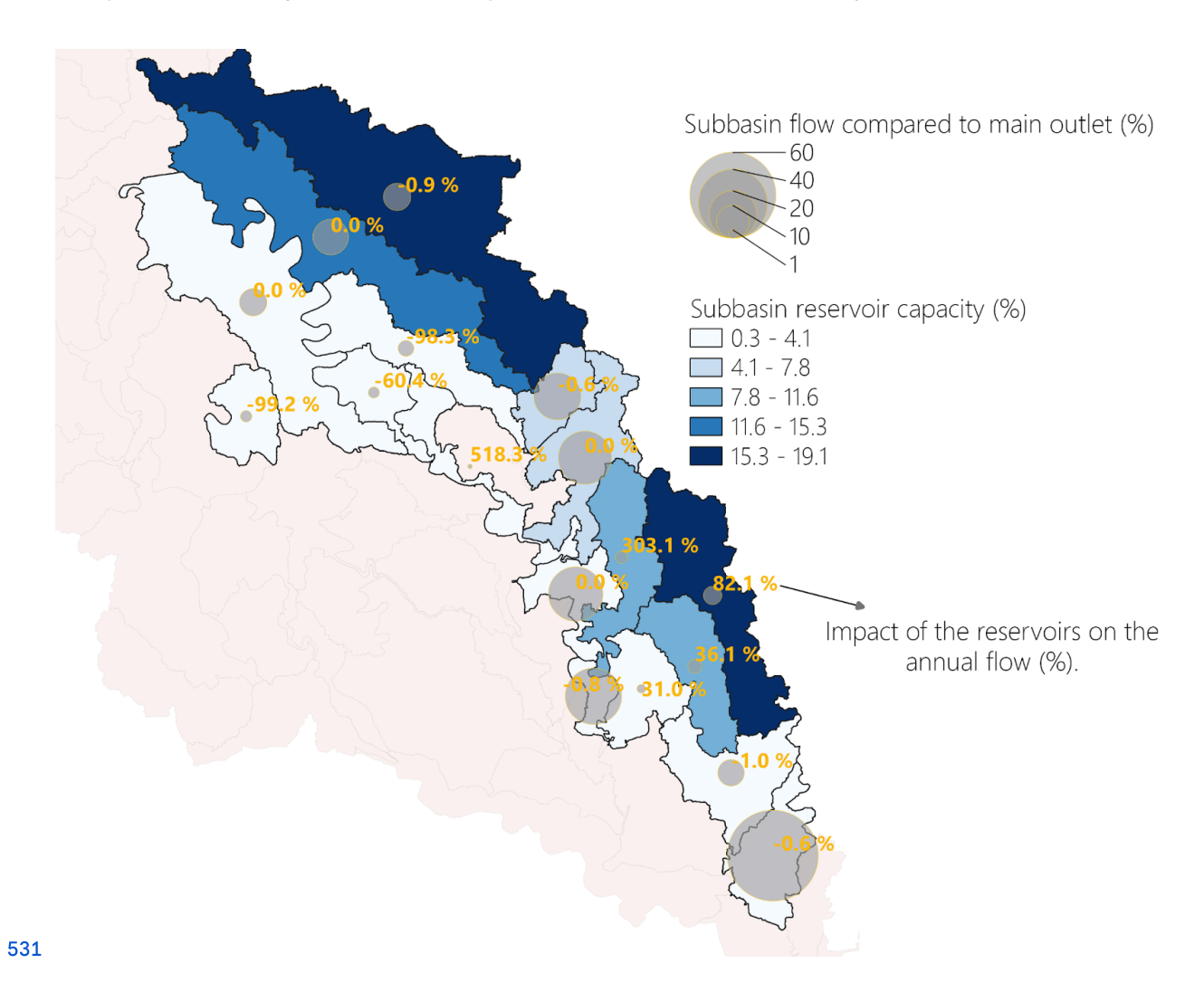


Figure 9–The cumulative impact of OFRs on annual flow for the mean scenario at the subwatersheds where the OFRs occurred. The size of the circles represents the contribution (%) of the subwatershed flow compared to the main outlet (i.e., model outlet). The subwatersheds are color coded according to their reservoir capacity (%), which was calculated by summing the OFRs surface area in each subwatershed and dividing the sum to the total OFRs surface area (i.e., including all OFRs from all subwatersheds), darker color indicating higher reservoir capacity. The percentages highlighted in yellow represent the impact of the OFRs on annual flow.

540 To assess the overall impact of the OFRs at the subwatershed level, we calculated the 541 contribution of each subwatershed flow to the main model outlet, and the subwatersheds' 542 reservoir capacity (i.e., summing the OFRs surface area at each subwatershed and dividing it 543 to the total OFRs surface area, including all OFRs from all subwatersheds) (Fig. 9). In general, 544 the highest impacts on annual flow (e.g., > 100%), with positive or negative magnitude, 545 occurred at the subwatersheds that contributed the least (< 10%) to the main model 546 outlet—these subwatersheds are represented in lighter shades of blue, and the annual 547 impact is highlighted in yellow on Fig. 9. In other words, the highest impacts on flow occurred 548 on the channels with smaller flow magnitudes (e.g., channels that presented mean flow 549 ranging between 0.001–0.25 and 0.25–0.50 m<sup>3</sup>/s, these channels were classified as class 1 and 550 2 in this study). In addition, the subwatersheds with the highest reservoir capacities (between 551 15.3 and 19.1 %, represented in darker shades of blue) (Fig. 9), had a small (< 10%) contribution 552 to the model outlet, and these subwatersheds did not present the highest impact on annual 553 flow (e.g., the impact on annual flow for the top two subwatersheds in terms of reservoir 554 capacity were -0.9 and 82.1%).

### 556 4 Discussion

Although OFRs will contribute to improve food production resilience—by providing surface water to irrigation during dry periods—to severe drought events, which are expected to have fighter occurrence with climate change, OFRS can have cumulative impacts on surface hydrology of the watershed where they occur. Studies have used either data-driven or physically-based hydrological model approaches to estimate OFR impacts on watersheds. However, combining these approaches provides a better understanding of the spatial and temporal variability of OFR impacts, as it incorporates the dynamic changes of OFRs into the hydrological model. Studies have either used data driven or physically based hydrological model approaches to estimate OFR impacts on the watersheds, despite the fact that temporal variability of the OFR impacts, given that the dynamic changes of the OFRs are temporal variability of the OFR impacts, given that the dynamic changes of the OFRs are incorporated into the hydrological model. To quantify whether the impact of the OFRs on mean and peak flow varied intra- and inter-annually, and which subwatersheds are more impacted, here we combined a data-driven remote sensing-based model with SWAT+ latest improvements to assess the OFR impacts.

## 572 4.1 Cumulative impact of OFRs

When simulating water impoundments in SWAT/SWAT+, it is common practice to validate and calibrate the model using flow measurements (Evenson et al., 2018; Habets et al., 575 2018; Jalowska & Yuan, 2019; Ni & Parajuli, 2018). In addition, other studies have validated and calibrated the model using alternative variables. For example, Perrin et al., (2012) employed monthly measurements of piezometric variations to assess aquifer recharge processes, and Jalowska & Yuan (2019) used sediment loadings (concentration and budget), from field monitoring reports to evaluate sediment simulations. Ideally, we would calibrate and validate the model by accounting for the parameters governing the OFRs' water budget (e.g., inflows

and outflows) (e.g., Kim and Parajuli, 2014). Nonetheless, these measurements were not available for the OFRs in our study region. Furthermore, a thorough calibration and validation of the model would require extra flow data, covering other parts of the study region, as the three USGS stations—the only data available—used in this study are located in the upper part of the modeled watershed. Similar to Evenson et al., (2018)—who proposed a module to better represent spatially distributed wetlands, and validated their model using a direct (i.e., flow measurement) and an indirect (i.e., the wetlands surface area) approach—our validation and calibration was done using the flow measurements, and the OFRs surface area scenarios were based on an algorithm that was validated with an independent higher spatial resolution dataset (Perin et al., 2022).

There is a consensus within the scientific community that the OFRs will have a 591 592 cumulative impact on surface hydrology by decreasing flow and peak flow, and the impact 593 will vary from watershed to watershed due to the number of OFRs, and the OFRs' different 594 purposes (e.g., different irrigation schedule) (Ayalew et al., 2017; Fowler et al., 2015; Habets et 595 al., 2018; Nathan & Lowe, 2012; Pinhati et al., 2020; Rabelo et al., 2021). As pointed out by Habets 596 et al., (2018) the mean annual decrease in flow from all studies was -13.4% ± 8%. Our results are 597 aligned with this value, which varied between -24.2 ± 4% and -14.6 ± 3% for all flow classes. In 598 addition, OFRs can reduce peak flow on average by 45% (Habets et al., 2018; Nathan and 599 Lowe, 2012; Thompson, 2012), and up to 70% (Ayalew et al., 2017) for certain flow events. 600 Likewise, our results are consistent with these findings, in which the mean impact on peak 601 flow varied between -60.7 ± 12% and -43.9 ± 12%. Furthermore, differently from previous 602 research, our results showed that the OFRs may have a positive (< 9%) impact on flow (Fig. 5, 603 classes 3 and 4). This could be explained by the level of details in our analyses. When 604 evaluating flow changes at the channel scale, it's important to note that flow at this level is 605 several orders of magnitude smaller than at the main basin outlet. Consequently, this scale 606 often exhibits more significant percentage changes, both increases and decreases. This likely 607 explains how OFRs can enhance channel flow, primarily due to the additional water 608 contributed by OFRs, influenced by periods of increased precipitation in certain channels 609 during specific months and years. While we calculated the monthly impact on flow at the 610 channel scale by aggregating the OFRs to the closest channel, previous studies have mostly 611 reported the annual impact on flows (Habets et al., 2018), and they performed their analysis at 612 the subwatershed scale by aggregating the OFRs to a single point at the outlet of each 613 subwatershed in SWAT (Evenson et al., 2018; Kim & Parajuli, 2014; Perrin, 2012; Zhang et al., 614 2012), or they used different modeling approaches (see Habet et al., (2018)).

By leveraging the latest improvements in SWAT+ to simulate water impoundments 615 616 (Molina-Navarro et al., 2018) in combination with a novel algorithm to monitor OFRs (Perin et 617 al., 2022), we modeled the impact of the OFRs on flow at the channel scale. In addition, the 618 surface area scenarios enabled us to account for events when the OFRs were at the lowest. 619 regular, and fullest capacities according to their surface area (see Fig. 2). This is an 620 improvement over previous studies (e.g., Ni et al., 2020; Ni and Parajuli, 2018; Perrin, 2012) that 621 used a single surface area (i.e., one snapshot in time) to represent the OFRs in SWAT. The 622 small differences (< 5%) between the surface area scenarios in terms of mean percent change 623 on monthly flow indicates that the OFRs' surface area variation had a low impact on flow. For 624 instance, during January and May the mean monthly percent change ranged between -35.8 ± 625 6% and -32.0  $\pm$  7%, and during June and December it varied between -8.8  $\pm$  5% and -5.4  $\pm$  6% 626 for the three surface area scenarios. The same was observed for peak flow, with a mean 627 monthly impact ranging between -52.7 ± 17% and -49.4 ± 18%. This small variability on flow 628 impact was observed even though the total OFR surface area increased by 590 ha and 1194 ha 629 when comparing the lower scenario with the mean and upper scenarios (Fig. 5). However, the 630 OFRs represented a small portion (< 1%) of the total area of the modeled watershed (Fig. 1). 631 These findings are related to the fact that flow simulations are governed by several 632 hydrological processes (e.g., run-off, precipitation, evapotranspiration) besides the presence of 633 OFRs on the channel (Bieger et al., 2017; Dile et al., 2022; Arnold et al., 2012). In addition, when 634 assessing the percent change in flow at the channel scale, the differences in surface area

635 between the scenarios occurred at a lower magnitude when compared to the total OFRs 636 surface area. For instance, an OFR with surface area smaller than 10 ha, and with surface area 637 variations between 10 and 20% for the three scenarios, may not lead to differences (e.g., > 10%) 638 between the three scenarios.

### 639 4.2 OFRs impacts on flow and peak flow

640 Our findings highlight that the impacts of the OFRs on flow and peak flow have a 641 significant intra- and inter-annual variability (Figs. 5, 6, and 7), and the impacts vary according 642 to different OFRs and channels (Fig. 5). The largest impacts on flow occurred during the first 643 part of the year between January and May, the period of the year when the peak flows occur. 644 In addition, this time of the year also coincides with the period when the region receives most 645 of its precipitation (Perin et al., 2021b), and the OFRs are at their fullest capacity (i.e., OFRs 646 storing their maximum amount of water) (Perin et al., 2022). During the second part of the 647 year, we observed a milder mean percent change in flow for all flow classes and all scenarios, 648 and a greater variability in percent change, notably for the months of July and August (Fig. 5). 649 Moreover, most of the irrigation activities happen between June and September (Perin et al., 650 2021b, Yaeger et al., 2017), and it is when the OFRs are at their lowest capacities (i.e., storing 651 less water) (Perin et al., 2022), which could explain their moderate impact and higher 652 variability during these months—even though we are not accounting for the OFRs inflows 653 and outflows, and not simulating irrigation events. Additionally, the variability of the OFRs 654 impacts is related to the OFRs' physical properties (e.g., surface area and location in the 655 watershed). For example, the OFR surface area will have an impact on flow and peak flow, as 656 shown by the different surface area scenarios, and depending on where the OFR is located in 657 the watershed, given that it may be connected to lower or higher flow channels, which 658 contributes to their impact variability during the year (Figs. 4 and 5). Besides the OFRs' 659 physical properties, the built-in complexity of SWAT—when simulating the presence of the 660 OFRs and the various hydrological processes (e.g., run-off, precipitation, evapotranspiration) 661 governing the water cycle—contributes to the differences in the OFRs impacts. This
662 complexity is illustrated in Fig. 8 showing that the upper scenario can have a higher or lower
663 impact on flow when compared to the lower and mean scenarios.

When assessing the annual impact of the OFRs accounting for each subwatershed flow compared to the main model outlet flow, and each subwatershed reservoir capacity (Fig. 666 9), we found that even though the presence of the OFRs can have a significant impact on 667 flow (Figs. 5, 6, and 7), the highest impacts tend to occur on the subwatersheds that 668 contribute the least (< 10%) to the main model outlet. In general, the highest impacts occurred on the channels with smaller flow magnitudes, and the subwatersheds with the 670 highest reservoir capacities did not have the highest impact on flow. The changes in the 671 OFRs impacts along the year, and between different years, are directly related to the OFRs 672 water balance (Equation 3). The variations are primarily driven by the volume of water stored 673 by the OFRs, which is modeled at a daily scale, and it varies according to total daily 674 precipitation, evaporation, and seepage losses.

### 675 4.3 Research implications and applications to other study regions

Overall, we presented a new approach to quantitatively analyze the impact of a network of OFRs on mean and peak flow, and we described the various potential reasons behind the variability of the impacts. Our results indicate that OFRs do not have an equally distributed impact on mean and peak flow across the watershed. This variability is primarily influenced by differences in their size, water storage capacity, and their spatial distribution (i.e., their presence). Hence, assessing the OFRs location as well as their numbers across the watershed is important when aiming to manage the construction of new OFRs. In particular, the geospatial variability of the OFRs impacts could be taken into account by water agencies when planning and developing a network of OFRs, given it is possible to identify the areas that are under high pressure (e.g., regions with multiple OFRs that are having a significant

686 impact on flow), and to identify areas that could benefit from the construction of new OFRs, 687 targeting improvements on water resources management and irrigation activities.

688 Furthermore, even though the OFRs impacts may vary significantly in different 689 watersheds (Habets et al., 2018), our approach could be transferable to other places across the 690 world, as it integrates a top-drown data-driven remote sensing-based algorithm, which is 691 based on freely available and private Earth Observations datasets, with the latest SWAT+ 692 hydrological modeling developments. In addition, the widespread use of SWAT+ and its 693 open-source nature, is yet another factor contributing to the transferability of the novel 694 approach presented in this study. This is relevant as the number of OFRs is expected to 695 increase globally (Althoff et al., 2020; Habets et al., 2014; Habets et al., 2018; Krol et al., 2011; 696 Rodrigues et al., 2012), with a limited knowledge of how the OFRs may impact surface 697 hydrology in different watersheds, and under diverse environmental conditions. Finally, in 698 tandem with the OFRs' key role on irrigated food production, in part to adapt to climate 699 change (Habets et al., 2018) and to alleviate the pressure on surface and groundwater 700 resources (Vanthof & Kelly, 2019; Yaeger et al., 2017; Yaeger et al., 2018), their impacts on 701 surface hydrology need to be considered to avoid exacerbating the surface water stress 702 already intensified by climate change and population growth (Vörösmarty et al., 2010).

## 703 5 Future improvements

Future improvements should focus on how to better represent the OFRs water management (i.e., OFRs inflows and outflows) in SWAT+. Given that each OFR has an independent water balance, accounting for the OFRs water volume change would be a more realistic representation of the OFRs when compared to the three surface area scenarios tested in this study. Estimating the OFRs volume change can be done by combining the OFR surface area time series with area-elevation equations—these equations describe the OFRs' bathymetry, and allow volume estimation by inputting the OFRs' surface area (Liebe et al., 2005; Meigh, 1995; Sawunyama et al., 2006). After carefully assessing different methods to derive these

712 equations (Arvor et al., 2018; Avisse et al., 2017; Li et al., 2021; Meigh, 1995; Sawunyama et al., 713 2006; Vanthof & Kelly, 2019; Yao et al., 2018; Zhang et al., 2016), we decided that measured 714 ground-data of the OFRs' depth—which is not available—is required to estimate the 715 equations with an acceptable uncertainty. Estimating the area-elevation equations entails 716 several challenges, including: 1) despite the fact that there are several DEMs available for the 717 study region (Arkansas GIS Office, 2022)—DEMs can be used to estimate the OFRs bottom 718 elevation—the DEMs were collected when most of the OFRs were full (i.e., bathymetry was 719 not exposed), which limits their use in this case; and 2) although the OFRs are located within 720 the same geomorphological region, they have different depth, shape and physical 721 characteristics (Perin et al., 2022; Yaeger et al., 2017). Therefore, even if a generalized 722 area-elevation equation was calculated for our study region—this is a common approach 723 done by other studies (Mady et al., 2020; Vanthof and Kelly, 2019)—that would still lead to high 724 uncertainties of water volume changes. Ideally, each OFR would have its own equation, which 725 was not possible when this study was done.

Efforts should also be made to improve SWAT+ capabilities to receive measured OFRs' representation of small water impoundments in SWAT+ (Mollina-Navarro et al., 2018). Nonetheless, at the time of our study, the newest version of the model does not allow users to rapid input measured or calculated OFRs' inflows and outflows. Instead, the model developers recommend simulating the OFRs water balance using decision tables (Arnold et al., 2018; Dile rate al., 2022). However, there are very limited guidelines on how to create these decision tables. Tables and or calculated volume change, which could introduce more uncertainties to the modeling rate scenarios. In addition, future work should integrate data on actual evapotranspiration, ET (Kiptala et al., 2014) to quantify as the balance between water availability and ET determines rate in large part the irrigation system efficiency and crop productivity in the watersheds where

### 739 6 Conclusions

740 We proposed a novel approach that combines a top-down data driven remote sensing-based 741 algorithm with the latest developments in SWAT+ to simulate the cumulative impacts of 742 OFRs. This enabled us to assess the spatial and temporal variability of the OFRs impacts, as 743 well as the intra- and inter-annual impact changes on mean and peak flow, at the watershed 744 and subwatershed levels. Incorporating Earth Observation derived information with a 745 hydrological model, allowed us to capture the dynamic changes of the OFRs, and to simulate 746 their impacts under different OFR capacity scenarios.

Our study showed that the OFRs may have an impact on flow and peak flow, which can have a significant inter- and intra-annual variability. The impact of the OFRs is not equally distributed across the watershed, and it varies according to the OFRs spatial distribution, and their surface area (i.e., water storage capacity). As the number of OFRs is expected to increase globally—partially to adapt to climate change and to alleviate pressure on groundwater resources—and therefore, also increase their relevance to irrigated food production, it is imperative to develop new frameworks to further understand the OFRs impacts on surface hydrology. In this regard, we provided a combination of different methods that can be used in other watersheds, which can support water agencies with information to improve surface water resources management.

## 757 7 Author contribution

758 VP, MGT planned study, analyzed data and modeling, and wrote and reviewed the759 manuscript. SF and AS carried out software analyses, wrote and reviewed. MLR and MAY data760 curation, wrote and reviewed.

## 761 8 Competing interests

762 The contact author has declared that none of the authors has any competing interests.

# 763 9 Acknowledgments

- 764 The first author was supported by NASA through the Future Investigators in NASA Earth and
- 765 Space Science and Technology fellowship.

## 766 10 Data Availability

- 767 The Soil Water Assessment Tool (SWAT) hydrological model and all necessary tools to perform
- 768 calibration, validation, and data analyses can be accessed through SWAT's online portal:
- 769 https://swat.tamu.edu/.
- 770
- 771 The National Land Cover Database (30 m) (Homer et al., 2020) and the Gridded Soil Survey
- 772 Geographic Database (gSSURGO) (Soil Survey Staff, USDA-NRCS, 2021) (100 m) are accessible
- 773 through the USGS's portal:
- 774 https://www.usgs.gov/centers/eros/science/national-land-cover-database, and here
- 775 https://www.nrcs.usda.gov/resources/data-and-reports/gridded-soil-survey-geographic-gssurg
- 776 o-database, respectively.
- 777
- 778 The climate data extracted from the Gridded Surface Meteorological Datasets (Abatzoglou,
- 779 2013) is available in Google Earth Engine (Gorelick et al., 2017), here
- 780 https://developers.google.com/earth-engine/datasets/catalog/IDAHO\_EPSCOR\_GRIDMET.
- 781
- 782 The Kalman filter derived surface area time series is available through Perin et al., (2022).

#### 783 10 References

- 784
- 785 Abatzoglou, J. T.: Development of gridded surface meteorological data for ecological
- 786 applications and modelling, Int. J. Climatol., 33, 121–131, https://doi.org/10.1002/joc.3413, 2013. 787
- 788 Althoff, D., Rodrigues, L. N., and da Silva, D. D.: Impacts of climate change on the evaporation
- 789 and availability of water in small reservoirs in the Brazilian savannah, Clim. Change, 159,
- 790 215-232, https://doi.org/10.1007/s10584-020-02656-y, 2020.
- 791
- 792 Arkansas GIS Office: Arkansas GIS Office | Elevation datasets, 2022.
- 793 Arnold, J. G., Moriasi, D. N., Gassman, P. W., Abbaspour, K. C., M. J. White, M. J., Srinivasan, R.,
- 794 Santhi, C., Harmel, R. D., van Griensven, A., Van Liew, M. W., Kannan, N., and Jha, M. K.: SWAT:
- 795 Model Use, Calibration, and Validation, Trans. ASABE, 55, 1491–1508,
- 796 https://doi.org/10.13031/2013.42256, 2012.
- 797
- 798 Arnold, J. G., Bieger, K., White, M. J., Srinivasan, R., Dunbar, J. A., and Allen, P. M.: Use of
- 799 Decision Tables to Simulate Management in SWAT+, Water, 10, 713,
- 800 https://doi.org/10.3390/w10060713, 2018.
- 801
- 802 Arvor, D., Daher, F. R. G., Briand, D., Dufour, S., Rollet, A.-J., Simões, M., and Ferraz, R. P. D.:
- 803 Monitoring thirty years of small water reservoirs proliferation in the southern Brazilian
- 804 Amazon with Landsat time series, ISPRS J. Photogramm. Remote Sens., 145, 225-237,
- 805 https://doi.org/10.1016/j.isprsjprs.2018.03.015, 2018.
- 806
- 807 Avisse, N., Tilmant, A., Müller, M. F., and Zhang, H.: Monitoring small reservoirs' storage with
- 808 satellite remote sensing in inaccessible areas, Hydrol. Earth Syst. Sci., 21, 6445-6459,
- 809 https://doi.org/10.5194/hess-21-6445-2017, 2017.

```
810
811 Ayalew, T. B., Krajewski, W. F., Mantilla, R., Wright, D. B., and Small, S. J.: Effect of Spatially
812 Distributed Small Dams on Flood Frequency: Insights from the Soap Creek Watershed, J.
813 Hydrol. Eng., 22, 04017011, https://doi.org/10.1061/(ASCE)HE.1943-5584.0001513, 2017.
814
815 Bieger, K., Arnold, J. G., Rathjens, H., White, M. J., Bosch, D. D., Allen, P. M., Volk, M., and
816 Srinivasan, R.: Introduction to SWAT+, A Completely Restructured Version of the Soil and
817 Water Assessment Tool, JAWRA J. Am. Water Resour. Assoc., 53, 115–130,
818 https://doi.org/10.1111/1752-1688.12482, 2017.
820 Canter, L. W. and Kamath, J.: Questionnaire checklist for cumulative impacts, Environ. Impact
821 Assess. Rev., 15, 311-339, https://doi.org/10.1016/0195-9255(95)00010-C, 1995.
822 Chalise, D. R., Sankarasubramanian, A., and Ruhi, A.: Dams and Climate Interact to Alter River
823 Flow Regimes Across the United States, Earth's Future, 9,
824 https://doi.org/10.1029/2020EF001816, 2021.
826 SWAT+ Toolbox: https://celray.github.io/docs/swatplus-toolbox/v1.0/index.html, last access: 17
827 June 2022.
828
829 Chawanda, C. J., Arnold, J., Thiery, W., and van Griensven, A.: Mass balance calibration and
830 reservoir representations for large-scale hydrological impact studies using SWAT+, Clim.
831 Change, 163, 1307–1327, https://doi.org/10.1007/s10584-020-02924-x, 2020.
832
833 Culler, R. C., Hadley, R. F., and Schumm, S. A.: Hydrology of the upper Cheyenne River basin:
834 Part A. Hydrology of stock-water reservoirs in upper Cheyenne River basin; Part B. Sediment
835 sources and drainage-basin characteristics in upper Cheyenne River basin, U.S. Geological
836 Survey, https://doi.org/10.3133/wsp1531, 1961.
837
838 Dile, Y., Srinivasan, R., and George, C.: QGIS Interface for SWAT+: QSWAT+, 2022.
840 Döll, P., Fiedler, K., and Zhang, J.: Global-scale analysis of river flow alterations due to water
841 withdrawals and reservoirs, Hydrol. Earth Syst. Sci., 13, 2413–2432,
842 https://doi.org/10.5194/hess-13-2413-2009, 2009.
844 Downing, J. A.: Emerging global role of small lakes and ponds: little things mean a lot,
845 Limnetica, 29, 9-24, https://doi.org/10.23818/limn.29.02, 2010.
846 Dubreuil, P. and Girard, G.: Influence of a very large number of small reservoirs on the annual
847 flow regime of a tropical stream, Wash. DC Am. Geophys. Union Geophys. Monogr. Ser., 17,
848 295–299, 1973.
849
850 Irrigation & Water Use:
851 https://www.ers.usda.gov/topics/farm-practices-management/irrigation-water-use/, last
852 access: 30 October 2021.
853
854 Entekhabi, D., Njoku, E. G., O'Neill, P. E., Kellogg, K. H., Crow, W. T., Edelstein, W. N., Entin, J. K.,
855 Goodman, S. D., Jackson, T. J., Johnson, J., Kimball, J., Piepmeier, J. R., Koster, R. D., Martin, N.,
856 McDonald, K. C., Moghaddam, M., Moran, S., Reichle, R., Shi, J. C., Spencer, M. W., Thurman, S.
857 W., Tsang, L., and Van Zyl, J.: The Soil Moisture Active Passive (SMAP) Mission, Proc. IEEE, 98,
858 704–716, https://doi.org/10.1109/JPROC.2010.2043918, 2010.
859
860 Evenson, G. R., Jones, C. N., McLaughlin, D. L., Golden, H. E., Lane, C. R., DeVries, B., Alexander,
```

861 L. C., Lang, M. W., McCarty, G. W., and Sharifi, A.: A watershed-scale model for depressional 862 wetland-rich landscapes, J. Hydrol. X, 1, 100002, https://doi.org/10.1016/j.hydroa.2018.10.002,

```
863 2018.
864
865 Farr, T. G., Rosen, P. A., Caro, E., Crippen, R., Duren, R., Hensley, S., Kobrick, M., Paller, M.,
866 Rodriguez, E., Roth, L., Seal, D., Shaffer, S., Shimada, J., Umland, J., Werner, M., Oskin, M.,
867 Burbank, D., and Alsdorf, D.: The Shuttle Radar Topography Mission, Rev. Geophys., 45,
868 https://doi.org/10.1029/2005RG000183, 2007.
869
870 Fowler, K., Morden, R., Lowe, L., and Nathan, R.: Advances in assessing the impact of hillside
871 farm dams on streamflow, Australas. J. Water Resour., 19, 96–108,
872 https://doi.org/10.1080/13241583.2015.1116182, 2015.
874 Galéa, G., Vasquez-Paulus, B., Renard, B., and Breil, P.: L'impact des prélèvements d'eau pour
875 l'irrigation sur les régimes hydrologiques des sous-bassins du Tescou et de la Séoune (bassin
876 Adour-Garonne, France), Rev. Sci. Eau J. Water Sci., 18, 273–305,
877 https://doi.org/10.7202/705560ar, 2005.
878
879 George, C.: Using SSURGO soil data with QSWAT and QSWAT+, 2020.
880 Gorelick, N., Hancher, M., Dixon, M., Ilyushchenko, S., Thau, D., and Moore, R.: Google Earth
881 Engine: Planetary-scale geospatial analysis for everyone, Remote Sens. Environ., 202, 18–27,
882 https://doi.org/10.1016/j.rse.2017.06.031, 2017.
883
884 Habets, F., Philippe, E., Martin, E., David, C. H., and Leseur, F.: Small farm dams: Impact on river
885 flows and sustainability in a context of climate change, Hydrol. Earth Syst. Sci., 18, 4207-4222,
886 https://doi.org/10.5194/hess-18-4207-2014, 2014.
888 Habets, F., Molénat, J., Carluer, N., Douez, O., and Leenhardt, D.: The cumulative impacts of
889 small reservoirs on hydrology: A review, Sci. Total Environ., 643, 850-867,
890 https://doi.org/10.1016/j.scitotenv.2018.06.188, 2018.
892 Homer, C., Dewitz, J., Jin, S., Xian, G., Costello, C., Danielson, P., Gass, L., Funk, M., Wickham, J.,
893 Stehman, S., Auch, R., and Riitters, K.: Conterminous United States land cover change patterns
894 2001–2016 from the 2016 National Land Cover Database, ISPRS J. Photogramm. Remote Sens.,
895 162, 184–199, https://doi.org/10.1016/j.isprsjprs.2020.02.019, 2020.
897 Hwang, J., Kumar, H., Ruhi, A., Sankarasubramanian, A., and Devineni, N.: Quantifying
898 Dam-Induced Fluctuations in Streamflow Frequencies Across the Colorado River Basin, Water
899 Resour. Res., 57, https://doi.org/10.1029/2021WR029753, 2021.
900
901 Jalowska, A. M. and Yuan, Y.: Evaluation of SWAT Impoundment Modeling Methods in Water
902 and Sediment Simulations, JAWRA J. Am. Water Resour. Assoc., 55, 209–227,
903 https://doi.org/10.1111/1752-1688.12715, 2019.
905 Jones, S. K., Fremier, A. K., DeClerck, F. A., Smedley, D., Pieck, A. O., and Mulligan, M.: Big data
906 and multiple methods for mapping small reservoirs: Comparing accuracies for applications in
907 agricultural landscapes, Remote Sens., 9, https://doi.org/10.3390/rs9121307, 2017.
908
909 Justice, C. O., Vermote, E., Townshend, J. R. G., Defries, R., Roy, D. P., Hall, D. K., Salomonson, V.
910 V., Privette, J. L., Riggs, G., Strahler, A., Lucht, W., Myneni, R. B., Knyazikhin, Y., Running, S. W.,
911 Nemani, R. R., Zhengming Wan, Huete, A. R., van Leeuwen, W., Wolfe, R. E., Giglio, L., Muller, J.,
912 Lewis, P., and Barnsley, M. J.: The Moderate Resolution Imaging Spectroradiometer (MODIS):
913 land remote sensing for global change research, IEEE Trans. Geosci. Remote Sens., 36,
914 1228–1249, https://doi.org/10.1109/36.701075, 1998.
```

```
916 Kalman, R. E.: A new approach to linear filtering and prediction problems, 1960.
```

- 917 Kennon, F. W.: Hydrologic effects of small reservoirs in Sandstone Creek Watershed, Beckham
- 918 and Roger Mills Counties, western Oklahoma, U.S. G.P.O., 1966.
- 919 Khazaei, B., Read, L. K., Casali, M., Sampson, K. M., and Yates, D. N.: GLOBathy, the global lakes
- 920 bathymetry dataset, Sci. Data, 9, 36, https://doi.org/10.1038/s41597-022-01132-9, 2022.

921

- 922 Kiptala, J.K., M.L. Mul, Y. Mohamed and P. van der Zaag, 2014. Modelling stream ow and
- 923 quantifying blue water using modified STREAM model for a heterogeneous, highly utilized
- 924 and data-scarce river basin in Africa. Hydrol. Earth Syst. Sci. 18, 2287-2303,
- 925 https://doi:10.5194/hess-10-18-2287-2014

926

- 927 Kim, H. K. and Parajuli, P. B.: Impacts of Reservoir Outflow Estimation Methods in SWAT Model
- 928 Calibration, Trans. ASABE, 1029-1042, https://doi.org/10.13031/trans.57.10156, 2014.

929

- 930 Krol, M. S., de Vries, M. J., van Oel, P. R., and de Araújo, J. C.: Sustainability of Small Reservoirs
- 931 and Large Scale Water Availability Under Current Conditions and Climate Change, Water

932

- 933 Resour. Manag., 25, 3017–3026, https://doi.org/10.1007/s11269-011-9787-0, 2011.
- 934 Li, Y., Gao, H., Allen, G. H., and Zhang, Z.: Constructing Reservoir Area-Volume-Elevation Curve
- 935 from TanDEM-X DEM Data, IEEE J. Sel. Top. Appl. Earth Obs. Remote Sens., 14, 2249-2257,
- 936 https://doi.org/10.1109/JSTARS.2021.3051103, 2021.

937

- 938 Liebe, J., van de Giesen, N., and Andreini, M.: Estimation of small reservoir storage capacities in
- 939 a semi-arid environment, Phys. Chem. Earth, 30, 448-454,
- 940 https://doi.org/10.1016/j.pce.2005.06.011, 2005.

941

- 942 Mady, B., Lehmann, P., Gorelick, S. M., and Or, D.: Distribution of small seasonal reservoirs in
- 943 semi-arid regions and associated evaporative losses, Environ. Res. Commun., 2, 061002,
- 944 https://doi.org/10.1088/2515-7620/ab92af, 2020.

945

- 946 Meigh, J.: The impact of small farm reservoirs on urban water supplies in Botswana, Nat.
- 947 Resour. Forum, 19, 71-83, https://doi.org/10.1111/j.1477-8947.1995.tb00594.x, 1995.

948

- 949 Molina-Navarro, E., Nielsen, A., and Trolle, D.: A QGIS plugin to tailor SWAT watershed
- 950 delineations to lake and reservoir waterbodies, Environ. Model. Softw., 108, 67–71,
- 951 https://doi.org/10.1016/j.envsoft.2018.07.003, 2018.

952

- 953 Moriasi, D. N., Gitau, M. W., Pai, N., and Daggupati, P.: Hydrologic and water quality models:
- 954 Performance measures and evaluation criteria, Trans. ASABE, 58, 1763–1785,
- 955 https://doi.org/10.13031/trans.58.10715, 2015.

956

- 957 Muche, M. E., Sinnathamby, S., Parmar, R., Knightes, C. D., Johnston, J. M., Wolfe, K., Purucker,
- 958 S. T., Cyterski, M. J., and Smith, D.: Comparison and Evaluation of Gridded Precipitation
- 959 Datasets in a Kansas Agricultural Watershed Using SWAT, JAWRA J. Am. Water Resour. Assoc.,
- 960 56, 486-506, https://doi.org/10.1111/1752-1688.12819, 2020.

961

- 962 Mukhopadhyay, S., Sankarasubramanian, A., and de Queiroz, A. R.: Performance Comparison
- 963 of Equivalent Reservoir and Multireservoir Models in Forecasting Hydropower Potential for
- 964 Linking Water and Power Systems, J. Water Resour. Plan. Manag., 147, 04021005,
- 965 https://doi.org/10.1061/(ASCE)WR.1943-5452.0001343, 2021.

- 967 Nash, J. E. and Sutcliffe, J. V.: River flow forecasting through conceptual models part I A
- 968 discussion of principles, J. Hydrol., 10, 282–290, https://doi.org/10.1016/0022-1694(70)90255-6,

```
969 1970.
 970
 971 Nathan, R. and Lowe, L.: The Hydrologic Impacts of Farm Dams, Australas. J. Water Resour., 16,
 972 75-83, https://doi.org/10.7158/13241583.2012.11465405, 2012.
 973 Census of agriculture: https://www.nass.usda.gov/AgCensus/index.php, last access: 10
 974 February 2021.
 975
 976 Ni, X. and Parajuli, P. B.: Evaluation of the impacts of BMPs and tailwater recovery system on
 977 surface and groundwater using satellite imagery and SWAT reservoir function, Agric. Water
 978 Manag., 210, 78–87, https://doi.org/10.1016/j.agwat.2018.07.027, 2018.
 979
 980 Ni, X., Parajuli, P. B., and Ouyang, Y.: Assessing Agriculture Conservation Practice Impacts on
 981 Groundwater Levels at Watershed Scale, Water Resour. Manag., 34, 1553–1566,
 982 https://doi.org/10.1007/s11269-020-02526-3, 2020.
 983
 984 Ogilvie, A., Belaud, G., Massuel, S., Mulligan, M., Le Goulven, P., Malaterre, P.-O., and Calvez, R.:
 985 Combining Landsat observations with hydrological modelling for improved surface water
 986 monitoring of small lakes, J. Hydrol., 566, 109–121, https://doi.org/10.1016/j.jhydrol.2018.08.076,
 987 2018.
 988
 989 Ogilvie, A., Poussin, J.-C., Bader, J.-C., Bayo, F., Bodian, A., Dacosta, H., Dia, D., Diop, L., Martin,
 990 D., and Sambou, S.: Combining Multi-Sensor Satellite Imagery to Improve Long-Term
 991 Monitoring of Temporary Surface Water Bodies in the Senegal River Floodplain, Remote Sens.,
 992 12, 3157, https://doi.org/10.3390/rs12193157, 2020.
 994 Perin, V., Roy, S., Kington, J., Harris, T., Tulbure, M. G., Stone, N., Barsballe, T., Reba, M., and
 995 Yaeger, M. A.: Monitoring Small Water Bodies Using High Spatial and Temporal Resolution
 996 Analysis Ready Datasets, Remote Sens., 13, 5176, https://doi.org/10.3390/rs13245176, 2021a.
 998 Perin, V., Tulbure, M. G., Gaines, M. D., Reba, M. L., and Yaeger, M. A.: On-farm reservoir
 999 monitoring using Landsat inundation datasets, Agric. Water Manag., 246, 106694,
1000 https://doi.org/10.1016/j.agwat.2020.106694, 2021b.
1001
1002 Perin, V., Tulbure, M. G., Gaines, M. D., Reba, M. L., and Yaeger, M. A.: A multi-sensor satellite
1003 imagery approach to monitor on-farm reservoirs, Remote Sens. Environ.,
1004 https://doi.org/10.1016/j.rse.2021.112796, 2022.
1005
1006 Perrin, J.: Assessing water availability in a semi-arid watershed of southern India using a
1007 semi-distributed model, J. Hydrol., 13, 2012.
1008
1009 Pinhati, F. S. C., Rodrigues, L. N., and Aires de Souza, S.: Modelling the impact of on-farm
1010 reservoirs on dry season water availability in an agricultural catchment area of the Brazilian
1011 savannah, Agric. Water Manag., 241, 106296, https://doi.org/10.1016/j.agwat.2020.106296, 2020.
1013 PRISM Gridded Climate Data: https://prism.oregonstate.edu/, last access: 2 January 2022.
1014 Rabelo, U. P., Dietrich, J., Costa, A. C., Simshäuser, M. N., Scholz, F. E., Nguyen, V. T., and Lima
1015 Neto, I. E.: Representing a dense network of ponds and reservoirs in a semi-distributed
1016 dryland catchment model, J. Hydrol., 603, 127103, https://doi.org/10.1016/j.jhydrol.2021.127103,
1017 2021.
1018
1019 Renwick, W. H., Smith, S. V., Bartley, J. D., and Buddemeier, R. W.: The role of impoundments in
1020 the sediment budget of the conterminous United States, Geomorphology, 71, 99-111,
```

1021 https://doi.org/10.1016/j.geomorph.2004.01.010, 2005.

```
1022
1023 Rodrigues, L. N., Sano, E. E., Steenhuis, T. S., and Passo, D. P.: Estimation of Small Reservoir
1024 Storage Capacities with Remote Sensing in the Brazilian Savannah Region, Water Resour.
1025 Manag., 26, 873–882, https://doi.org/10.1007/s11269-011-9941-8, 2012.
1026
1027 Sawunyama, T., Senzanje, A., and Mhizha, A.: Estimation of small reservoir storage capacities in
1028 Limpopo River Basin using geographical information systems (GIS) and remotely sensed
1029 surface areas: Case of Mzingwane catchment, Phys. Chem. Earth Parts ABC, 31, 935-943,
1030 https://doi.org/10.1016/j.pce.2006.08.008, 2006.
1031
1032 Schreider, S. Yu., Jakeman, A. J., Letcher, R. A., Nathan, R. J., Neal, B. P., and Beavis, S. G.:
1033 Detecting changes in streamflow response to changes in non-climatic catchment conditions:
1034 farm dam development in the Murray-Darling basin, Australia, J. Hydrol., 262, 84-98,
1035 https://doi.org/10.1016/S0022-1694(02)00023-9, 2002.
1036
1037 Soil Survey Staff, USDA-NRCS: Gridded Soil Survey Geographic (gSSURGO) Database for the
1038 Conterminous United States. United States Department of Agriculture, Natural Resources
1039 Conservation Service., 2021.
1041 Publications | Soil & Water Assessment Tool (SWAT): https://swat.tamu.edu/publications/, last
1042 access: 17 June 2022.
1043
1044 Tapley, B. D., Bettadpur, S., Watkins, M., and Reigber, C.: The gravity recovery and climate
1045 experiment: Mission overview and early results, Geophys. Res. Lett., 31, n/a-n/a,
1046 https://doi.org/10.1029/2004GL019920, 2004.
1047
1048 Thompson, J. C.: Impact and Management of Small Farm Dams in Hawke's Bay, New Zealand,
1049 thesis, Open Access Te Herenga Waka-Victoria University of Wellington,
1050 https://doi.org/10.26686/wgtn.16997929.v1, 2012.
1051
1052 United States Geological Survey Water Data for the Nation: https://waterdata.usgs.gov/nwis,
1053 last access: 22 June 2022.
1054
1055 Van Den Hoek, J., Getirana, A., Jung, H., Okeowo, M., and Lee, H.: Monitoring Reservoir Drought
1056 Dynamics with Landsat and Radar/Lidar Altimetry Time Series in Persistently Cloudy Eastern
1057 Brazil, Remote Sens., 11, 827, https://doi.org/10.3390/rs11070827, 2019.
1059 Van Der Zaag, P. and Gupta, J.: Scale issues in the governance of water storage projects, Water
1060 Resour. Res., 44, https://doi.org/10.1029/2007WR006364, 2008.
1061
1062 Vanthof, V. and Kelly, R.: Water storage estimation in ungauged small reservoirs with the
1063 TanDEM-X DEM and multi-source satellite observations, Remote Sens. Environ., 235, 111437,
1064 https://doi.org/10.1016/j.rse.2019.111437, 2019.
1066 Verpoorter, C., Kutser, T., Seekell, D. A., and Tranvik, L. J.: A global inventory of lakes based on
1067 high-resolution satellite imagery, Geophys. Res. Lett., 41, 6396-6402,
1068 https://doi.org/10.1002/2014GL060641, 2014.
1069
1070 Vörösmarty, C. J., McIntyre, P. B., Gessner, M. O., Dudgeon, D., Prusevich, A., Green, P., Glidden,
1071 S., Bunn, S. E., Sullivan, C. A., Liermann, C. R., and Davies, P. M.: Global threats to human water
1072 security and river biodiversity, Nature, 467, 555–561, https://doi.org/10.1038/nature09440, 2010.
```

1074 Yaeger, M. A., Reba, M. L., Massey, J. H., and Adviento-Borbe, M. A. A.: On-farm irrigation

- 1075 reservoirs in two Arkansas critical groundwater regions: A comparative inventory, Appl. Eng.
- 1076 Agric., 33, 869–878, https://doi.org/10.13031/aea.12352, 2017.

1077

- 1078 Yaeger, M. A., Massey, J. H., Reba, M. L., and Adviento-Borbe, M. A. A.: Trends in the
- 1079 construction of on-farm irrigation reservoirs in response to aquifer decline in eastern, Agric.
- 1080 Water Manag., 208, 373–383, https://doi.org/10.1016/j.agwat.2018.06.040, 2018.

1081

- 1082 Yao, F., Wang, J., Yang, K., Wang, C., Walter, B. A., and Crétaux, J. F.: Lake storage variation on
- 1083 the endorheic Tibetan Plateau and its attribution to climate change since the new
- 1084 millennium, Environ. Res. Lett., 13, https://doi.org/10.1088/1748-9326/aab5d3, 2018.

1085

- 1086 Yapo, P. O., Gupta, H. V., and Sorooshian, S.: Automatic calibration of conceptual rainfall-runoff
- 1087 models: sensitivity to calibration data, J. Hydrol., 181, 23–48,
- 1088 https://doi.org/10.1016/0022-1694(95)02918-4, 1996.

1089

- 1090 Yongbo, L., Wanhong, Y., Zhiqiang, Y., Ivana, L., Jim, Y., Jane, E., and Kevin, T.: Assessing Effects
- 1091 of Small Dams on Stream Flow and Water Quality in an Agricultural Watershed, J. Hydrol.
- 1092 Eng., 19, 05014015, https://doi.org/10.1061/(ASCE)HE.1943-5584.0001005, 2014.

1093

- 1094 Zhang, C., Peng, Y., Chu, J., Shoemaker, C. A., and Zhang, A.: Integrated hydrological modelling
- 1095 of small- and medium-sized water storages with application to the upper Fengman Reservoir
- 1096 Basin of China, Hydrol Earth Syst Sci, 15, https://doi.org/10.5194/hess-16-4033-2012, 2012.

- 1098 Zhang, S., Foerster, S., Medeiros, P., de Araújo, J. C., Motagh, M., and Waske, B.: Bathymetric
- 1099 survey of water reservoirs in north-eastern Brazil based on TanDEM-X satellite data, Sci. Total
- 1100 Environ., 571, 575-593, https://doi.org/10.1016/j.scitotenv.2016.07.024, 2016.